Revision 01

Word Count: 6793

Oxygen isotope ratios in zircon and garnet: A record of assimilation and fractional crystallization in the Dinkey Dome peraluminous granite, Sierra Nevada, CA

Raiza R. Quintero[1*], Kouki Kitajima[1], Jade Star Lackey[2], Reinhard Kozdon[1, 3], Ariel Strickland[1], and John W. Valley[1]

[1]WiscSIMS, Department of Geoscience, University of Wisconsin, Madison, WI, 53706, USA

[2] Geology Department, Pomona College Claremont, CA, 91711, USA

[3] Lamont-Doherty Earth Observatory of Columbia University, Palisades, NY, 10964, USA

For submission to *American Mineralogist* (John Valley Issue)

*Corresponding Author present address:

Space Science Technology Centre, School of Earth and Planetary Science, Curtin University of Technology GPO Box U1987, Perth, WA, 6845 Australia

r.quinteromendez@postgrad.curtin.edu.au

Abstract

The 119 Ma Dinkey Dome pluton in the central Sierra Nevada Batholith is a peraluminous granite and contains magmatic garnet and zircon that are complexly zoned with respect to oxygen isotope ratios. Intracrystalline SIMS analysis tests the relative importance of magmatic differentiation processes vs. partial melting of metasedimentary rocks. Whereas $\delta^{18}O$ values of bulk zircon concentrates are uniform across the entire pluton (7.7‰ VSMOW), zircon crystals are zoned in $\delta^{18}O$ by up to 1.8‰, and when compared to late garnet, show evidence of changing magma chemistry during multiple interactions of the magma with wall rock during crustal transit. The evolution from an early high-$\delta^{18}O$ magma [$\delta^{18}O$(WR) = 9.8‰] towards lower values is shown by high $\delta^{18}O$ zircon cores (7.8‰) and lower $\delta^{18}O$ rims (6.8‰). Garnets from the northwest side of the pluton show a final increase in $\delta^{18}O$ with rims reaching 8.1‰. In situ REE measurements show zircon is magmatic and grew before garnets. Additionally, $\delta^{18}O$ in garnets from the western side of the pluton are consistently higher (Ave = 7.3‰) relative to the west (Ave = 5.9‰).

These $\delta^{18}O$ variations in zircon and garnet record different stages of assimilation and fractional crystallization whereby an initially high $\delta^{18}O$ magma partially melted low $\delta^{18}O$ wallrock and was subsequently contaminated near the current level of emplacement by higher $\delta^{18}O$ melts. Collectively, the comparison of $\delta^{18}O$ zoning in garnet and zircon shows how a peraluminous pluton can be constructed from multiple batches of variably contaminated melts, especially in early stages of arc magmatism where magmas encounter significant heterogeneity of wall-rock assemblages. Collectively, peraluminous magmas in the Sierran arc are limited to small < 100 km^2 plutons that are intimately associated with metasedimentary wallrocks and often surrounded by later and larger, metaluminous tonalite and granodiorite plutons. The general

associations suggest that early stage arc magmas sample crustal heterogeneities in small melt batches, but that with progressive invigoration of the arc, such compositions are more effectively blended with mantle melts in source regions. Thus, peraluminous magmas provide important details of the nascent Sierran arc and pre-batholithic crustal structure.

Keywords: peraluminous granite, garnet, zircon, Sierra Nevada, oxygen isotopes, REE, SIMS

Introduction

The petrogenesis of peraluminous granites is a longstanding question (Clemens and Wall 1981; Patiño Douce and Johnston 1991; Frost et al. 2001; Villaros et al. 2009; Lackey et al. 2011). Peraluminous composition in granitoid rocks is defined by molar proportions of Al_2O_3 in excess of combined CaO, Na_2O, and K_2O: $Al_2O_3/(CaO+K_2O+Na_2O) > 1$, or an aluminum saturation index (ASI > 1; Zen 1988). Peraluminous granitoids typically form from a high proportion of melts of aluminous crustal or sedimentary source rocks (Chappell and White 1974; Scaillet et al. 2016). Alternative mechanisms can explain the generation of weakly peraluminous compositions in granitoid rocks (e.g. fractional crystallization, crustal anatexis and vapor phase transfer; Zen 1988).

Isotope tracers can discriminate between source, magmatic differentiation, and contamination characteristics of peraluminous magmas. Early work showed correlated $^{87}Sr/^{86}Sr$ and $\delta^{18}O$ as indicative of crustal melting (O'Neil and Chappell 1977; Halliday et al. 1981). Oxygen isotope ratios are affected by assimilation of crustal rocks, which have different $\delta^{18}O$ values than mantle-derived magmas (e.g., Taylor and Sheppard 1986; Valley et al. 2005). In cases where crustal melts are produced from young source rocks, radiogenic isotopes are not sensitive, and oxygen isotopes are typically the most sensitive isotopic tracer (e.g., Valley 2003; Lackey et al. 2011; Jeon et al. 2012).

Oxygen isotopes can be measured in retentive zoned minerals to record information about magma evolution (e.g., Valley 2003; Bindeman 2008; Lackey et al. 2011). Self-diffusion rates of oxygen in garnet and zircon are among the slowest in common minerals (Coughlan 1990; Wright et al. 1995; Watson and Cherniak 1997; Vielzeuf et al. 2005; Page et al. 2007a, 2010; Bowman et al. 2011), and crystallization of both minerals in peraluminous granites allows them to be used in tandem to record a more complete time history than would be provided by a single mineral (Lackey et al. 2011). The $\delta^{18}O$ values of zircon and garnet are quenched upon crystallization and growth zoning provides a record of magmatic evolution (King and Valley 2001; Valley 2003; Lackey et al. 2006).

Zircon and other accessory minerals also record the rare earth element (REE) compositions of felsic magmas during their growth (Sawka and Chappell 1988; Hoskin et al. 2000; Hoskin and Schaltegger 2003). Rare earths are incorporated in zircon by coupled substitution mechanisms (Speer 1982; Hinton and Upton 1991; Halden et al. 1993; Hoskin and Ireland 2000; Finch et al. 2001; Hoskin and Schaltegger 2003).

In this study, we employ secondary ion mass spectrometry (SIMS) to measure oxygen isotope ratios ($\delta^{18}O$) and trace element compositions, including Y + REEs. The SIMS method provided accurate and precise measurements of intracrystalline zoning at high spatial resolution (ca. 10 μm) in zircon and garnet crystals collected throughout the Dinkey Dome granite (Fig. 1). The zoning measured within these crystals is useful to contextualize contamination, assimilation, and/or high temperature alteration processes during growth of both zircon and garnet.

The resulting data constrain models for the origin and contamination of silicic melts in the Sierra Nevada batholith. The processes that formed this and other granites senso stricto in the Sierra are critical to understand the relative contribution of preexisting crust in the Sierran arc

and evaluate the different processes that affected the composition of final magmas. Thus, in situ analysis of refractory magmatic minerals helps in discriminating the relative amounts of crustal contribution by: crystal fractionation and partial melting of mafic magmas, where no crustal contribution is required in the production of felsic magmas (Ratajeski et al. 2001, 2005; Wenner and Coleman 2004); contamination, assimilation and fractional crystallization whereby magmas become silicic (Lackey et al., 2005, 2006, 2008; Nelson et al. 2013); and wholesale melting of crustal material by deep heat sources with no contribution of mafic material (Holden et al. 1987).

Geology

The Sierra Nevada Batholith

The voluminous Cretaceous Sierra Nevada batholith, California (Fig. 1) consists mainly of tonalite to granodiorite plutons to depths of ~35 km (Saleeby et al. 2003), with more mafic diorite and refractory gabbroic residues continuing to ca. 45 km (Fliedner et al. 2000). Gabbro complexes and mafic enclaves are a common but volumetrically small part of the batholith and have been targeted to study the mass balance of mantle and crustal melt inputs to produce the intermediate, granodiorite compositions that are the bulk of the batholith (Dorais et al. 1990; Coleman et al. 2004; Wenner and Coleman 2004). Other studies have examined the sub-arc mantle and residual mafic root of the batholith, sampled as pyroxenite, garnet-clinopyroxenite, and lherzolite xenoliths in Cenozoic volcanic rocks (Moore and Dodge 1980; Ducea 2001; Lee et al. 2006; Chin et al. 2014). Such studies provide additional information on mantle controls of magmatic heat budgets and mafic magma flux, revealing in detail that multi-stage crystallization and re-melting episodes are required to build granodioritic crust that complements the major element (e.g., Mg) and isotopic compositions of xenoliths. In addition, experimental studies

show that high silica melts can be produced from re-melting of Sierran gabbros (Sisson et al. 2005; Ratajeski et al. 2005)

Despite considerable attention to magmatic origins recorded in mafic to ultramafic rocks, few studies have focused on potential high-silica melts; $\delta^{18}O$ studies of granodiorite and tonalite suites require at least 15-30% input of melts from supracrustal sources, thus partial melting of gabbros is not the sole source of potential high-silica end-member melts. Thus, direct studies of rocks with relatively undiluted high-silica crustal melts are important, but only a handful have been undertaken: Wenner and Coleman (2004) studied several granites in a regional survey of both mafic and felsic plutons in the Sierra; Zeng et al. (2005) examined partial melting in a lower crustal migmatite complex in the Southern Sierra Nevada; Lackey et al. (2006) studied regional and pluton-scale patterns of $\delta^{18}O$ of peraluminous granites in the Sierra. These three studies found evidence of crustal melting in the granitic plutons and migmatites, highlighting the importance of such melts as a factor in the isotopic variability in many Sierran granodiorites, hence, added motivation to study the Dinkey Dome granite.

The Dinkey Dome granite

The garnet, two-mica Dinkey Dome granite is a relatively small (~30 km^2) pluton surrounded by granodiorite plutons (e.g., Dinkey Creek Granodiorite) and other granites of the Shaver Intrusive Suite (Figs. 1 and 2; Bateman 1992; Lackey et al. 2006). With a U-Pb zircon age of 119 Ma (Frazer et al. 2008), the Dinkey Dome pluton is coeval with the oldest members of the Fine Gold Intrusive Suite to the west, and significantly older than other members of the Shaver Intrusive Suite (Frazer et al. 2008). Thus, the Dinkey Dome represents a case of magmatism that was anomalously inboard of the broad magmatic "locus" in the Sierra at the time it was emplaced, and a departure from the broad trend of eastward-younging Cretaceous

intrusive suites in the Sierran Arc (Chen and Moore 1982; Memeti et al. 2010; Davis et al. 2012; Lackey et al. 2012; Ardill et al. 2018; Chapman and Ducea 2019). Initial $^{87}Sr/^{86}Sr$ ratios of the Dinkey Dome granite are 0.7065 (Kistler and Peterman 1973). Metamorphic wallrocks consist of quartzite, mica schist, biotite hornfels, and marble (Fig. 2) (Bateman and Wones 1972). The chemistry of the pluton and aluminous minerals (garnet, muscovite, Al_2SiO_5) contained therein are typical for peraluminous granites. Whole rock geochemical analyses of the Dinkey Dome show that aluminum saturation indices (ASI) are peraluminous (west side ASI = 1.02; east side ASI = 1.07; Lackey et al. 2006). Average garnet compositions in the Dinkey Dome granite are $Alm_{72.4}Sps_{19.5}Pyp_{5.8}Grs_{2.3}$ on the west and $Alm_{78.6}Sps_{19.1}Pyp_{0.9}Grs_{1.4}$ on the east. There are no garnet-bearing metamorphic wallrocks in contact with the Dinkey Dome, consistent with the magmatic origin of garnet (Lackey et al. 2011). Shallow crystallization is inferred by scattered miarolitic cavities in the east side of the pluton that are inferred to indicate a pressure of <1 kbar (Wones et al. 1969). The preservation of coarse, euhedral books of muscovite, suggests some of the muscovite formed at depth, and was preserved during ascent and final crystallization of the magma. The Dinkey Creek Granodiorite, which is ~8 million years younger than the Dinkey Dome granite (Frazer et al. 2008), engulfs the Dinkey Dome pluton and its pendant. Al-in-hornblende pressure estimates of the Dinkey Creek Granodiorite are 4.0 ±0.4 kbar, from 10 widely distributed samples collected by Ague and Brimhall (1988a) and recalculated by Tobisch et al. (1993). The pressures derived from hornblende in the Dinkey Creek Granodiorite imply considerable difference of depth, although, hornblende may just record early, deeper magmatic conditions which is plausible given increasing evidence of hornblende populations showing a continuum of magma conditions (Barnes et al. 2017). Nevertheless, the pressure/age differential implies 10 km of burial of the Dinkey Dome granite and its pendant rocks in 8 million years.

Construction of younger batholith rocks with higher apparent pressures around pendants and older plutons that are relatively shallow is seen elsewhere in the Sierra Nevada. For instance, recent oxygen isotope analysis of skarn garnets in the Mineral King pendant (85 km SE) shows paleo-hydrothermal systems were infiltrated by meteoric water at ca. 135 Ma (Ryan-Davis et al. 2019) and again at ca. 109 Ma (D'Errico et al. 2012), but that younger (98 Ma) voluminous granodiorite plutons surround the pendant and these hydrothermal systems record apparent emplacement pressures of ca. 3 kbar (Ague and Brimhall 1988b), deeper than the possible brittle-ductile transition that would permit extensive meteoric water circulation. Similarly, volcanic rocks in the Ritter Range pendant (60 km N) have steep, down-dip stretching lineations and are found adjacent to slightly younger plutonic rocks (Tobisch et al. 2000). This juxtaposition of younger shallow plutons against older, higher pressure rocks, suggests that the older rocks were engulfed by later magmas as the batholith is built around them through interplays of bulk-arc thickening, structural shortening, or a density driven settling (e.g., Glazner and Miller, 1997).

Petrography. The Dinkey Dome granite contains quartz, plagioclase, K-feldspar, zircon, biotite and muscovite, and commonly has garnet, perthite, sericitized feldspar, granophyre and myrmekite. Accessory phases include zircon, monazite, apatite, magnetite and ilmenite. Andalusite and sillimanite show scattered occurrence on the eastern side of the pluton (Guy, 1980). Molybdenite and uraninite have been reported on the eastern side as well (Lackey et al., 2006). Andalusite has textural traits indicative of magmatic crystallization, including uniformly sized and distributed, euhedral to subhedral grains free of carbonaceous chiastolite inclusions that are typically associated with metamorphic andalusite (Clarke et al. 2005). Where observed, fibrolitic sillimanite is uniformly distributed in the granite and does not appear to form at the expense of andalusite or vice versa. The concentration of fibrolite toward the interior of the

pluton was interpreted to record high temperatures in the interior of that domain that may have lasted longer. Guy (1980) also noted fine-grained, secondary muscovite replacing andalusite and sillimanite, likely forming under subsolidus conditions (Guy, 1980), unlike early, phenocrystic muscovite; thus, muscovite and aluminosilicates in the pluton likely integrate varying P-T conditions as magma ascended, was contaminated, and crystallized. Analyses of $\delta^{18}O$ (And) in two samples showed values consistent with magmatic crystallization; values of 8.5‰ are ~2‰ lower than pluton $\delta^{18}O$ (WR) values whereas adjacent wallrock $\delta^{18}O$ values are 3-4‰ higher than andalusite and inconsistent with high temperature equilibrium. Values of $\delta^{18}O$ of fibrolite from one sample are similar to co-existing andalusite, a result consistent with crystallization of the two minerals from the same magma (Lackey et al. 2006).

Garnet and Zircon: occurrence, morphology and internal structures. Magmatic garnet occurs throughout the Dinkey Dome and is found in all the samples collected in this study and by Lackey et al. (2006). Unlike other peraluminous plutons in the Sierra Nevada where garnet is concentrated near contacts, magmatic garnet in the Dinkey Dome occurs throughout the entire pluton. These crystals are generally subhedral to euhedral and range in size from 200-2000 μm. The pluton contains both pink and red garnet. Garnet in the west side of the pluton is darker (red) vs. lighter (pink) in the east side. BSE imaging reveals subtle concentric oscillatory growth-zoning within these grains. Garnet grains aren't generally inclusion-rich and the distribution of inclusions from grain-to-grain is not uniform throughout the samples. Garnet crystals contain inclusions of plagioclase, K-feldspar, muscovite, biotite, quartz, monazite, apatite, ilmenite and zircon (Fig. 3).

Zircon in the Dinkey Dome granite occurs as euhedral crystals that range in size from 20 to 300 μm but are generally ~100 μm long and 25-50 μm wide. In some cases, zircon crystals

occur as inclusions within garnet (Figs. 3c and d). Conversely, some zircon grains contain inclusions of quartz, K-feldspar, apatite, plagioclase, biotite, ilmenite, and magnetite that have been identified by EDS. Ortiz (2010) examined 50 zircons by SEM in a polished grain mount from sample 1S79 and found apatite inclusions in 9 zircon grains, K-feldspar in 8, quartz in 4, biotite in 2, and Fe-Ti oxide in 1. BSE and CL imaging reveals oscillatory zoning; convolute zoning is present in some zircon cores. Representative textures are seen in Figure 4.

Previous isotopic work

Lackey et al. (2006) analyzed $\delta^{18}O$ by laser fluorination of garnet (Grt), zircon (Zrn), quartz (Qz), andalusite (And) and whole rock powders (WR) in the Dinkey Dome pluton (Fig. 2) as part of a regional study of peraluminous granitoid plutons in the Sierra Nevada. Their study produced several key results. First, values of $\delta^{18}O$ are elevated: $\delta^{18}O(WR)$ = 9.6–10.4‰ VSMOW, $\delta^{18}O(Qz)$= 10.6–11.3‰, $\delta^{18}O(And)$= 8.4–8.5‰, $\delta^{18}O(Zrn)$= 7.0–7.8‰, and $\delta^{18}O(Grt)$= 6.7–7.4‰. The surrounding Kings Sequence metasedimentary rocks (marbles, hornfels, and quartzites) of the Dinkey Creek pendant have $\delta^{18}O(WR)$ of 9.5–11.6‰. Other peraluminous granites in the Sierra Nevada Batholith also have high $\delta^{18}O(Zrn)$ >7.5‰, while metaluminous granitic rocks near the Dinkey Dome have average zircon $\delta^{18}O$ values that range from 6.5–7.5‰ (Lackey et al. 2006, 2008).

Values of $\delta^{18}O$ for zircon, quartz and whole rock are unimodal across the entire pluton, however, $\delta^{18}O$ values of magmatic garnet are bimodal, decreasing by ~0.6‰ on the east side of the central metasedimentary septum within the Dinkey Dome (Fig. 2). High $\delta^{18}O$ values and equilibrium fractionations of garnet and zircon on the west side of the pluton ($\Delta^{18}O(Grt\text{-}Zrn)$ = 0.06 ±0.13‰), indicate that prior to the crystallization of both minerals, the magma was elevated in $\delta^{18}O$. On the eastern side, $\delta^{18}O$ values of garnet are lower and not equilibrated with zircon

($\Delta^{18}O(Grt\text{-}Zrn) = -0.6 \pm 0.13‰$), recording a change in magmatic $\delta^{18}O$ synchronous with crystallization. These differences in fractionation are small but distinct. The lower $\delta^{18}O$ values in garnet that formed later than zircons, seen as inclusions in garnet (Figs. 3c and d), suggest that low $\delta^{18}O$ material was assimilated after the crystallization of zircon and before crystallization of garnet. These results are interpreted to indicate that the Dinkey Dome granitic magmas evolved through contamination by low $\delta^{18}O$ material, however no low $\delta^{18}O$ country rocks are exposed in the Dinkey Creek Pendant. Thus, partial melting of such a low $\delta^{18}O$ contaminant would be required to have occurred deeper in the crust (Lackey et al. 2006).

Methods

Sample preparation and imaging

Zircon and garnet mineral separates of ten samples from Lackey et al. (2006) (samples 1S51 to 1S82) were handpicked and cast in 25-mm diameter round epoxy mounts along with the Kim-5 zircon (Valley 2003) and UWG-2 garnet (Valley et al. 1995) standards, ground to the level of best mineral exposure, polished to a smooth, flat, low-relief surface, and carbon coated prior to imaging. Secondary Electron (SE), Backscattered Electron (BSE) and Cathodoluminescence (CL) images were obtained for each grain, and Energy Dispersive X-ray Spectrometry (EDS) was conducted using the UW-Madison, Dept. of Geoscience Hitachi S-3400N SEM (Scanning Electron Microscope). Based on the images obtained, approximately 10 zircon grains (that display distinctive rims and cores) and five garnet grains were chosen for in situ analysis from each sample. The SEM images were also used to locate the positions for SIMS analyses. Carbon coats were then removed, and the mounts were coated with gold for SIMS analysis.

Twenty-five-mm round thin sections were made of samples collected during this study (samples 10DD02-10DD19, Table 1, Supplementary Table A) (Fig. 2) and top mounted with UWQ-1 quartz standard (Kelly et al. 2007) and UWG-2 in their centers. Isotopic analysis of minerals in thin section rather than in grain mounts permits detailed descriptions of zircon and garnet that are in known petrographic relation to each other. Imaging prior to SIMS analysis was conducted in the same manner as described above.

Major and minor element analyses of garnet by electron microprobe

Determination of composition and testing for compositional zoning preceded every SIMS $\delta^{18}O$ analysis of garnet. Major and minor element analyses of garnet were obtained using the UW-Madison, Dept. of Geoscience CAMECA SX51 electron microprobe by wavelength dispersive spectrometry. Eight elements were analyzed: Si, Al, Fe, Mg, Mn, Ca, Ti, and Cr (Supplementary Table B). The operating conditions were accelerating potential of 15KeV, 40° takeoff angle, and a fixed focused beam at 20 nA. Counting time for all elements was 10 seconds on-peak and 10 seconds off-peak. LIF, PET, and TAP analyzer crystals were used to acquire Kα X-ray intensities for Mn, Fe and Cr; Ca and Ti; and Al, Si and Mg, respectively. Crystalline standards were used: Minas Gerais rutile for Ti; U.W. synthetic fayalite for Fe; synthetic tephroite for Mn; USNM 143968 Kakanui pyrope for Mg; $Andradite_{99}$-Rota (Hungary) for Ca; synthetic Cr_2O_3 for Cr; and HU $Almandine_{56}$ for Al and Si.

Laser Fluorination analysis of $\delta^{18}O$

In order to assess any correlation of chemical composition with $\delta^{18}O$, individual garnet grains (~1.5-2.0 mg) from 10 samples previously studied by Lackey et al. (2006) were analyzed in the UW-Madison, Dept. of Geoscience Stable Isotope Laboratory by laser fluorination using BrF_5 as the reagent. A dual-inlet gas-source Finnigan/MAT 251 mass spectrometer was used to

measure isotope ratios. Standardization was done using UWG-2 ($\delta^{18}O$ = 5.80 ‰ VSMOW), which provides high precision and accuracy in laser analyses (Valley et al. 1995). Values of $\delta^{18}O$ of whole rock powders (~2mg) of Dinkey Dome granite and Dinkey Creek sedimentary rocks were analyzed by laser fluorination using an airlock sample chamber (Spicuzza et al. 1998) (Supplementary Table E).

SIMS analysis of $\delta^{18}O$ in garnet and zircon

Oxygen isotope ratios were measured at the WiscSIMS Laboratory, Department of Geoscience, UW-Madison with a CAMECA ims-1280 large-radius multicollector ion microprobe/SIMS (Kita et al. 2009; Valley and Kita 2009). Oxygen isotopes were analyzed using a 2.0–2.2 nA primary Cs^+ beam accelerated by 10 kV (impact energy = 20 kV) and focused on sample surface with ~10–12 μm spot diameter. Secondary ^{16}O and $^{18}O^-$ ions were measured by two Faraday cup detectors simultaneously. Zircon standard KIM-5 ($\delta^{18}O$ = 5.09 ‰ VSMOW; Valley 2003) and garnet standard UWG-2 ($\delta^{18}O$ = 5.80 ‰ VSMOW; Valley et al. 1995) were mounted in the center of each sample and used as running standards to bracket unknown sample analyses. Four consecutive measurements of the standard were made before and after every set of 10 sample analyses. Additional standardization and calibration of garnet standards was performed to account for the compositional effects on instrumental bias as described previously (Page et al. 2010, Russell et al. 2013, Kitajima et al. 2016). Typically, two analysis spots were made on each zircon (core and rim), and approximately 3-8 spots (rim to rim) on each garnet.

Cracks, inclusions, radiation-damaged zircon domains and other features that can compromise an analysis were avoided by secondary electron (SE), backscattered electron (BSE), and cathodoluminescence (CL) imaging of minerals before in situ analysis. In addition, all SIMS

pits were imaged post-analysis using BSE and SE, and pits that hit cracks or contain mineral inclusions are culled from the final dataset (Supplementary Tables C-D).

SIMS analysis of REEs in zircon

Zircon grains were analyzed by SIMS for trace elements, including rare earth elements (REEs) in the WiscSIMS Laboratory at UW-Madison with a CAMECA ims-1280. The following elements were analyzed: Li, Si, P, Ca, Ti, V, Fe, Y, La, Ce, Pr, Nd, Sm, Eu, Tb, Gd, Dy, Ho, Er, Tm, Yb, Lu, Hf, Th, and U (Supplementary Table F). Similar conditions as Page et al. (2007b) were used: impact energy of 23 kV, 4 nA O^- ion beam shaped to a diameter of 25 μm on the sample surface and a secondary ion accelerating voltage of 10 kV. For trace element analysis the configuration of the secondary ion optics was optimized for high transmission (Kita et al. 2009). A single electron multiplier, field aperture of 4000 μm, MRP of 3000, and secondary beam energy offset of 40 V were used and allow resolution of the selected REE peaks from the interfering REE oxides. Measured counts for each element were normalized to ^{30}Si. During the analysis session, NIST-610 glass was used as a running standard. To estimate the matrix effects on relative sensitivity factor (RSF) between zircon and NIST 610, the zircon standards 91500 (Y, REE, Hf, Th and U: Wiedenbeck et al. 2004) and Xinjiang (Li: Ushikubo et al. 2008) were analyzed at the beginning of the trace element session. For Ti concentration, we used the correction factor on RSF between zircon and NIST-610 reported by Fu et al. (2008). No correction for matrix effect was applied on P, Ca, V and Fe because their concentrations in the 91500 zircon are unknown. Counting times were adjusted for NIST-610 because of the difference in REE composition in comparison to natural zircons (Page et al. 2007b) (Supplementary Table F).

Results

Garnet composition by EPMA

Garnet grains from the Dinkey Dome pluton are almandine-spessartine-rich with minor pyrope and grossular (X_{Alm}= 0.60-0.86; X_{Sps} = 0.11-0.27; X_{Pyp} = 0.01-0.07; X_{Grs} = 0.02-0.06) **(**Fig. 5a). Most of the garnets analyzed in this study slightly increase in spessartine and decrease in almandine at the rims. Internal cation zoning is generally subtle, however crystals 1S52-02, 1S52-04, 1S80-04, and 10DD07b-02 show bell-shaped rim-to-rim profiles. Compositionally, garnet is similar to garnet from other Sierran granitoids (Guy and Wones 1980, Calk and Dodge 1986, Ague and Brimhall 1988a, Liggett 1990; Lackey et al. 2006). Values of X_{Grs} are higher in western side of the pluton, suggesting slightly higher crystallization pressures. Crystals from the eastern side of the pluton have less pyrope and are generally more almandine-rich (Fig. 5a), which can explain the difference in color east to west.

Oxygen isotope ratios by Laser Fluorination

Laser fluorination analyses of oxygen isotope ratios in garnet from a west to east traverse (A-A', Fig. 2 and 6) were conducted to assess variations between pink garnet (lower X_{Alm}) and red garnet. Only one of the samples analyzed (1S51) shows a variation in $\delta^{18}O$ between red (7.25 ±0.23‰ 2SD) and pink garnet (6.80 ±0.23‰); the other samples showing different color grains (1S77, 1S79, and 1S82) show no variation in $\delta^{18}O$.

Individual garnets from samples 1S51, 1S52, 1S53, 1S77, 1S79, 1S80, and 1S81 were handpicked and analyzed by both laser fluorination and SIMS (Supplementary Table E). Values of $\delta^{18}O$ obtained by laser fluorination for these grains average 6.90 ±0.18‰ (1SD) for the eastern side and 7.63 ±0.17‰ to the west. These values are similar to those obtained Lackey et al. (2006), who also reported lower $\delta^{18}O$ for garnet from the eastern part of the pluton.

This is the peer-reviewed, final accepted version for American Mineralogist, published by the Mineralogical Society of America.
The published version is subject to change. Cite as Authors (Year) Title. American Mineralogist, in press.
DOI: https://doi.org/10.2138/am-2021-7472. http://www.minsocam.org/

Whole rock analyses where also made of granite and metasediment samples 10DD-02 through 10DD-22 (Table 1). The granite $\delta^{18}O$(WR) values range from 9.0 to 10.5‰, and the metasedimentary rocks (biotite hornfels and quartzite) range in $\delta^{18}O$(WR) from 11.7 to 12.8‰.

Oxygen isotope ratios by SIMS

Garnet. Garnets from the western side of the pluton analyzed by SIMS resemble the laser fluorination analysis (within uncertainty). In contrast, garnets from the eastern side of the pluton show consistently lower values relative to laser fluorination analysis, with a difference of $\delta^{18}O$ values ranging from 0.6 to 1.5‰ (Fig. 6b) (Table 1). These differences likely result from quartz inclusions within garnet crystals that are higher in $\delta^{18}O$ and were unavoidably analyzed by laser fluorination. The SIMS analyses avoid inclusions that are plainly visible in polished surfaces and thus SIMS values of $\delta^{18}O$ are not affected by inclusions.

Values of $\delta^{18}O$ in epoxy-mounted garnet grains from western side of the pluton are higher (average $\delta^{18}O$(Grt) = 7.4 ±0.2‰) than eastern side $\delta^{18}O$(Grt) values of 6.3 ±0.2‰, and show no significant core to rim zoning in $\delta^{18}O$. Average values of $\delta^{18}O$ measured from garnets selected in thin section show a similar trend with higher values on the western side (6.9 ±0.3‰) and lower values on the eastern side (5.2 ±0.3‰). However, unlike garnet hand-picked from mineral separates, garnets in thin section show variation in $\delta^{18}O$ from rims to cores (Fig.7). The core to rim variation is more prominent on the larger (>1 mm) garnets from the northwestern side of the pluton. The zoning of the eastern-side garnets is more subtle and less common (Table 1).

This difference likely results due to analysis of larger subhedral garnets in thin section rather than the smaller equant garnets that were selected from mineral separates. It is also possible that the low $\delta^{18}O$ garnets are more delicate and were destroyed by the disk mill during sample processing. The $\delta^{18}O$ in garnets from thin sections on the east side is very low (ave. = 5.2

±0.3‰). This pattern, combined with the observation of large miarolitic cavities in the east side of the pluton suggests the possibility of the garnet rims growing into the sub-solidus realms, with some non-magmatic water infiltrating the system. Studies of Cretaceous skarns in the south-central Sierra show that garnet growing in shallow hydrothermal systems may record multiple episodes of fluid flow and low-$\delta^{18}O$ domains record incursions of meteoric water at different times, including waning stages of garnet growth (e.g., D'Errico et al. 2012; Ryan-Davis et al. 2019). Therefore, the Dinkey Dome garnet may record some surface water infiltration on the East side.

Zircon. SIMS analyses of rims and cores of individual zircon grains from 10 Dinkey Dome samples along the A-A' traverse (Fig. 2, 1S51-1S82) show constant $\delta^{18}O$ values for the cores: 7.8 ±0.3‰ on the east side and 7.7 ±0.3‰ on the west side. The rims of the zircons have consistently lower $\delta^{18}O$ values that average 6.7 ±0.3‰ on the east side and 6.9 ±0.3‰ on the west side (Fig. 6a).

SIMS $\delta^{18}O$ values of zircon in thin sections from the eastern side average 7.2 ±0.2‰ (Fig. 6a, Table 1). The average $\delta^{18}O$ in each zircon from the western part of the pluton is 7.6 ±0.2‰. These values are consistent with SIMS data for zircon cores (7.7 to 7.8‰) that dominate the mass of each zircon. Zircons from some samples (10DD-02a-b, 10DD-05a, 10DD-16c, 10DD-17, and 10DD-19c) did not have rims that were distinguishable by CL.

Trace elements in zircon

Trace element compositions in cores and rims of grains from the Dinkey Dome granite are summarized in chondrite-normalized REE diagrams (Fig. 8). The REE data are consistent with igneous zircon from continental crust (Belousova et al. 1998; Hoskin and Ireland 2000;

Belousova et al. 2002, Grimes et al. 2007) and show HREE enrichment, a positive Ce anomaly and a negative Eu anomaly (Fig. 8).

All zircon data plot within the 'magmatic' field in REE discriminant diagrams: $(Sm/La)_N$ vs. La (ppm) and Ce/Ce* ($(Ce)_N/\sqrt{((La)_N(Pr)_N)}$ vs. $(Sm/La)_N$ (Figs. 9a and b). None of the cores or rims have REE compositions similar to hydrothermal zircon (Hoskin 2005). Although Chondrite normalized REE patterns are similar in cores and rims of grains (Fig. 8), $(Sm/La)_N$ vs. La (ppm) and Ce/Ce* vs. $(Sm/La)_N$ are clearly bimodal, with rims having slightly flatter LREEs and being higher in [La] and lower $(Sm/La)_N$, (Figs. 9a and 9b).

Discussion

Causes of $\delta^{18}O$ zoning

The in situ measurements of $\delta^{18}O$ and trace elements from magmatic garnet and zoned zircon grains reveal a more complex magmatic history of assimilation and fractional crystallization for the Dinkey Dome granite than was resolved by bulk-mineral analysis. High-$\delta^{18}O$ zircon cores crystallized from an initially high-$\delta^{18}O$ magma derived by melting of a high-$\delta^{18}O$ source deeper in the crust (Figs. 10 and 11). The zircon cores average 7.7‰, indicating $\delta^{18}O$(magma) values of 9.4‰ [~69 wt. % SiO_2; $\Delta^{18}O$(WR-Zrc) ≈ 0.0612 (wt.% SiO_2) – 2.5‰ (Lackey et al. 2008)]. The inclusions of zircon in garnet and the steep positive slope of HREEs in zircon indicate that the majority of garnet grew after zircon. Lower $\delta^{18}O$ values in the rims of zircon (ave. 6.8‰) and throughout most garnets show that a lower $\delta^{18}O$ contaminant, possibly hydrothermally altered rocks, contributed some low-$\delta^{18}O$ melt into parts of the magma at depth. Quartz from the Dinkey Dome and whole rocks (including feldspars) do not record such low $\delta^{18}O$ values (Lackey et al. 2006), however absence of low-$\delta^{18}O$ values in quartz and feldspar could arise from exchange of oxygen isotopes between these minerals with igneous fluids

411 contributed from younger, more voluminous magmas (e.g., the 101 Ma Dinkey Creek
412 Granodiorite) that engulfed the Dinkey Dome pluton and its aureole. The assimilation and
413 fractional crystallization history of Dinkey Dome magma thus appears preferentially preserved in
414 zircon and garnet due to the minerals' slower diffusion rates relative to quartz and feldspar.
415 It is significant that no low $\delta^{18}O$ (< 5‰) rocks are identified in the pendant immediately
416 adjacent to the Dinkey Dome pluton. Thus, the lower $\delta^{18}O$ domains in garnet and zircon point to
417 this stage of melting and contamination of the magma at depths greater than final crystallization
418 depths. The wallrock in the Sierran arc is heterogeneous by nature, containing domains of
419 Triassic and Jurassic hydrothermally altered volcanic wallrocks with relatively low $\delta^{18}O$ (e.g.,
420 Peck and Van Kooten 1983; D'Errico et al. 2012; Ryan-Davis et al. 2019). Such metavolcanic
421 and metasedimentary wallrocks are the most likely source of a low-$\delta^{18}O$ assimilation signature.
422 Evidence of melting is found where migmatite complexes are developed in metavolcanics rocks
423 at mid- to lower-crustal level pendants in the southern Sierra Nevada (Saleeby et al. 2003).
424 Nevertheless, thermal budgets of peraluminous magma should limit significant melting and
425 assimilation of wallrock at emplacement levels of the Dinkey Dome pluton, or mixing of
426 magmas, thus the low-$\delta^{18}O$ assimilation may be restricted to a thin veneer of the eastern half of
427 the pluton, where garnets record the lowest $\delta^{18}O$ values. The eastern part is also at a higher
428 elevation, and thus it is possible the isotopic signatures are restricted to a thin copula (Fig. 11),
429 and/or that the isotopic signatures of the eastern side are correlative to rocks eroded away from
430 the western side. Discrete zoning is shown by the heterogeneous nature of the Dinkey Dome
431 pluton; the northwestern samples show a rim-ward shift to higher $\delta^{18}O$ in some garnet rims
432 suggesting that as some of the magma was produced and transported, it encountered high-$\delta^{18}O$
433 rock and was locally contaminated (Fig. 11).

Episodic contamination of a peraluminous magma

The findings from this work also raise the question of how, given their small size and limited thermal budgets, high silica magmas may episodically interact with wallrocks in arc crust. This process is partially illustrated at the pluton scale by the Hall Canyon pluton in the Panamint Range, California (Mahood et al. 1996). Here, a roof zone with pegmatitic and aplitic domains is enriched in peraluminous minerals (garnet, muscovite) compared to lower in the pluton, however the entire pluton is peraluminous. The authors invoke in situ fractionation of the magma in the upper roof zone with additional melts also percolating up into the roof zone from the lower reaches of the pluton. In such a scenario, fractionating melt increases peraluminosity (such as seen in the eastern Dinkey Dome pluton) and promotes additional growth of peraluminous minerals (e.g. garnet, sillimanite, and andalusite). Because fractionating peraluminous magmas sees increased concentrations of water and incompatible elements, this fractionation would counteract the tendency of cooling and crystallization to impede distribution of new melt into the "mushy" roof zone of the pluton (e.g., Scaillet et al. 2000). A similar process might have occurred in the eastern Dinkey Dome pluton whereby a more highly fractionated roof zone continued to receive melts and consequently achieved the isotopic heterogeneity seen in crystal-scale $\delta^{18}O$ zoning that was not recorded in the western domain. Sustained melt and fluid percolation in the east side also could have allowed low-$\delta^{18}O$ values to be recorded in some generations of garnet that continued to grow as peraluminosity increased. In contrast, the west side of the pluton crystallized deeper and relatively earlier and thus did not record incorporation of the low-$\delta^{18}O$ material and thus was more homogeneous in its composition. Thus, the east and west sides of the Dinkey Dome pluton behaved as two magma batches, separated by a septum of metasediments, that accumulated, fractionated, and ultimately

457 crystallized.

458 **Timing and preservation of crustal melts in arcs**

459 Given that the Dinkey Dome pluton was emplaced into its pendant rocks earlier than other
460 plutons in the Shaver Intrusive suite, it would have been emplaced inboard of the main locus of
461 magmatism in the arc, and likely encountered a thicker, more heterogeneous crustal column and
462 interactions with that crust superimposed additional contamination on the magma. The Dinkey
463 Dome is not the only example in the region. The Grant Grove peraluminous granite, which
464 shares similarities with Dinkey Dome, like being isolated by pendant rocks and surrounded by
465 younger metaluminous plutons, shows higher $\delta^{18}O$ in its margin indicative of localized
466 contamination (Lackey et al. 2006). That localized "veneer" of later contamination is manifested
467 by additional growth of garnet and aluminosilicates at the margin of the pluton where it intruded
468 and partially melted schists near emplacement levels.

469 Although of Jurassic age, peraluminous plutons that intrude the Julian Schist in the
470 Peninsular Ranges batholith in southern California are comparable (Shaw et al. 2003). These
471 granites are relatively small compared the younger (Cretaceous) tonalite and granodiorite plutons
472 that surround them, comprising most of the Peninsular Ranges batholith. Some of the Jurassic
473 plutons are directly associated with migmatitic zones in the Julian Schist and have elevated Sr_i
474 (>0.71) and $\delta^{18}O$ (16-20‰), values that overlap with the schist itself indicating it was the source
475 of the melts that produced the peraluminous plutons. Though of much greater age difference than
476 the Dinkey Dome and younger plutons that surround it and associated pendant rocks, the
477 progression from early, small peraluminous plutons to larger metaluminous plutons is the same.
478 Unlike the Peninsular Ranges example, the Dinkey Dome does not have evidence of a localized
479 migmatite complex, consistent with its final shallow (low pressure) emplacement, although there

480 is evidence produced of migmatite complexes in lower crustal exposures in the Sierra (Zeng et
481 al. 2005). In addition, the peraluminous plutons of the Peninsular Ranges contain abundant,
482 Proterozoic zircon cores and crystals (Shaw et al. 2003), likely because melts from which they
483 crystallized were saturated in zirconium and unable to dissolve grains inherited from their
484 metasedimentary sources (e.g., Miller et al. 2003). The Dinkey Dome granite contains few
485 inherited cores (Fig. 4). It follows is that the Dinkey Dome magmas were potentially derived
486 from hotter or inheritance-poor sources (Miller et al. 2003) and presumably are farther separated
487 from said source(s) that might be analogous to those in migmatite complexes in the southern
488 Sierra (Zeng et al. 2005).

489 Overall, a theme emerges from the Mesozoic arc segments in California, wherein small
490 volume peraluminous melts are the primary archive of melts of crustal "character," but that these
491 melts are restricted to earlier magmatism. It follows that because these antecedent magmas form
492 in early stages of magmatism, as heat content in the arc is ramping, they may have sustained
493 mobility, which allows them to preserve more chemical heterogenity. The increased vigor of arc
494 magmatism also means that such crustal melt expression is muted in younger arc plutons. These
495 later stages are typified by periods of high-flux magmatism from more organized sources that
496 efficiently homogenize magmas with greater proportions of mantle melts (Lackey et al. 2012).

497 **Conclusions and Implications**

498 Contrasting records of isotopic heterogeneity in zircon and garnet crystals within
499 different domains of the Dinkey Dome pluton exemplify how: 1) Sierran felsic granitoids
500 originate though a variety of processes and are not restricted to end member models; and 2)
501 early-stage plutons record crustal melting in the nascent stages of arc magmatism. The evolution
502 of early-stage Sierran granitoids reflects intermediate processes whereby magmas became more

503 felsic due to a combination of processes such as contamination, assimilation and fractional
504 crystallization at different stages (Lackey et al., 2005, 2006, 2008; Nelson et al. 2013). The
505 requirement for an enriched-mantle model whereby granites are derived solely by several stages
506 of partial melting and fractionation of these enriched-mantle sources, with no crustal input
507 (Coleman and Glazner 1997; Ratajeski et al. 2001, 2005), need not be so restrictive given the
508 high oxygen isotopic values recorded in cores of zircon grains ($\delta^{18}O$ =7.7 to 7.8‰) in the Dinkey
509 Dome pluton. Instead, before an arc organizes a Melting-Assimilation-Storage-and
510 Homogenization (MASH) system, hot zone (Annen et al. 2006), or similar magmatic source
511 region capable of homogenizing unusual melt compositions, peraluminous plutonic "harbingers"
512 like Dinkey Dome sample the pre-batholithic crustal structure. This crustal melt sampling period
513 is brief and rare, but may be echoed in later stages arc stages when tectonic adjustments to the
514 arc reposition crustal rocks into sites of melting (e.g., DeCelles et al. 2009), but also created
515 conditions that are favorable to preserve such melts in structurally and thermally isolated regions
516 of arcs such as in shear zones and metamorphic wallrock complexes. As a case in point, the shut-
517 down of the Sierran arc is accompanied by a structural disruption of the arc and introduction of
518 fertile schists into the subduction channel that are expressed as late stage, small-volume, high
519 $\delta^{18}O$ peraluminous melts (Chapman et al. 2013). Other intervals, such as during a major re-
520 organization within the arc at 105 Ma saw an increase in $\delta^{18}O$ and $^{87}Sr/^{86}Sr$ consistent with a
521 crustal melting episode (Holland et al. 2013). Thus, peraluminous plutons in arcs, though small
522 and temporally restricted, record important aspects of the greater tectono-magmatic feedback
523 systems and can potentially be used to identify cryptic crustal end members that become greatly
524 diluted in more vigorous stages of arc magmatism produce the typical voluminous granodiorite.
525

Acknowledgements

The authors thank Noriko Kita and the WiscSIMS group for SIMS analysis, John Fournelle for EPMA, Mike Spicuzza for laser fluorination, Brian Hess for polishing samples, and Adam Kinnard for help in the field. We also thank Chris Harris and an anonymous reviewer for constructive and detailed reviews that improved the paper, and William Peck for editorial comments. This study was supported by a BP plc–University of Wisconsin Research Assistantship, the DOE 93ER14389 and NSF EAR-0838058 (JWV), and NSF EAR-0948706 (JSL). WiscSIMS is supported by National Science Foundation (EAR-1658823) and the University of Wisconsin – Madison.

References

Ague, J.J., and Brimhall, G.H. (1988a) Regional variations in bulk chemistry, mineralogy, and the compositions of mafic and accessory minerals in the batholiths of California. Geological Society of America Bulletin, 100, 891–911.

Ague, J.J., and Brimhall, G.H. (1988b) Magmatic arc asymmetry and distribution of anomalous plutonic belts in the batholiths of California: effects of assimilation, crustal thickness, and depth of crystallization. Geological Society of America Bulletin, 100, 912–927.

Ardill, K., Paterson, S., and Memeti, V. (2018) Spatiotemporal magmatic focusing in upper-mid crustal plutons of the Sierra Nevada arc. Earth and Planetary Science Letters, 498, 88–100.

Annen, C., Blundy, J.D., and Sparks, R.S.J. (2006) The genesis of intermediate and silicic magmas in deep crustal hot zones: Journal of Petrology, 47, 505–539.

Barnes, C.G., Berry, R., Barnes, M.A., Ernst, W.G. (2017) Trace element zoning in hornblende: tracking and modeling the crystallization of a calc-alkaline arc pluton. American Mineralogist, 102, 2390-2405.

549 Bateman, P.C. (1992) Plutonism in the central part of the Sierra Nevada batholith, California.
550 USGS Professional Paper, 1483, 186 p.
551 Bateman, P.C., and Wones, D.R. (1972) Geologic map of the Huntington lake quadrangle,
552 central Sierra Nevada, California. USGS Geologic Quadrangle Map 987.
553 Belousova, E.A., Griffin, W.L., and Pearson, N.J. (1998) Trace element composition and
554 cathodoluminescence properties of southern African kimberlitic zircons. Mineralogical
555 Magazine, 62, 355–366.
556 Belousova, E.A., Griffin, W.L., O'Reilly, S.Y, and Fisher, N.I. (2002) Igneous zircon: trace
557 element composition as an indicator of source rock type. Contributions to Mineralogy and
558 Petrology, 143, 602–622.
559 Bindeman, I.N. (2008) Oxygen Isotopes in Mantle and Crustal Magmas as Revealed by Single
560 Crystal Analysis. Reviews in Mineralogy and Geochemistry, 69, 445–478.
561 Bowman, J.R., Moser, D.E., Valley, J.W., Wooden, J.L., Kita, N.T., and Mazdab, F.K. (2011)
562 Zircon U-Pb isotope, $\delta^{18}O$ and trace element response to 80 m.y. of high temperature
563 formation. American Journal of Science, 311, 719–772.
564 Calk, L.C., and Dodge, F.C. (1986) Garnet in granitoid rocks of the Sierra Nevada Batholith,
565 California. 14th International Mineralogical Association, Abstracts, p. 69.
566 Chapman, J.B., and Ducea, M.N. (2019) The role of arc migration in Cordilleran orogenic
567 cyclicity. Geology, 47, 627–631.
568 Chapman, A.D., Saleeby, J.B., and Eiler, J. (2013) Slab flattening trigger for isotopic disturbance
569 and magmatic flare-up in the southernmost Sierra Nevada Batholith, California. Geology,
570 41(9), 1007-1010.

571 Chappell, B.W., and White, A.J.R. (1974) Two contrasting granite types. Pacific Geology, 8,
572 173–174.
573 Chen J.H., and Moore J.G. (1982) Uranium-lead isotopic ages from the Sierra Nevada batholith,
574 California. Journal of Geophysical Research, 87, 4761–4784.
575 Chin, E.J., Lee, C.T.A., and Barnes, J.D. (2014) Thickening, refertilization, and the deep
576 lithosphere filter in continental arcs: Constraints from major and trace elements and oxygen
577 isotopes. Earth and Planetary Science Letters, 397, 184-200.
578 Clarke, D.B., Dorais, M., Barbarin, B., Barker, D., Cesare, B., Clarke, G., El Baghdadi, M.,
579 Erdmann, S., Forster, H.J., Gaeta, M., and others (2005) Occurrence and Origin of
580 Andalusite in Peraluminous Felsic Igneous Rocks. Journal of Petrology 46, 441–472.
581 Clemens, J.D., and Wall, V.J. (1981) Origin and crystallization of some peraluminous (S-type)
582 granitic magmas. Canadian Mineralogist, 19, 111–131.
583 Coleman, D.S., and Glazner, A.F. (1997) The Sierra Crest magmatic event: rapid formation of
584 juvenile crust during the late Cretaceous in California. International Geological Review, 39,
585 768–787.
586 Coleman, D.S., Gray, W., and Glazner, A.F. (2004) Rethinking the emplacement and evolution
587 of zoned plutons: Geochronologic evidence for incremental assembly of the Tuolumne
588 Intrusive Suite, California. Geology, 32, 433–436.
589 Coughlan, R.A. (1990) Studies in diffusional transport: grain boundary transport of O in
590 feldspars, diffusion of O, strontium, and the REEs in garnet and thermal histories of granitic
591 intrusions in south-central Maine using O isotopes, 476 p. Ph.D. thesis, Brown University,
592 Providence.
593 Davis, J.W., Coleman, D.S., Gracely, J.T., Gaschnig, R., and Stearns, M. (2012) Magma

accumulation rates and thermal histories of plutons of the Sierra Nevada batholith, CA. Contributions to Mineralogy and Petrology, 163, 449–465.

DeCelles, P.G., Ducea, M.N., Kapp, P., and Zandt, G. (2009) Cyclicity in Cordilleran orogenic systems. Nature Geoscience, 2, 251-257.

D'Errico, M.E., Lackey, J.S., Surpless, B.E., Loewy, S.L., Wooden, J.L., Barnes, J.D., Strickland, A., and Valley, J.W. (2012) A detailed record of shallow hydrothermal fluid flow in the Sierra Nevada magmatic arc from low-$\delta^{18}O$ skarn garnets. Geology, 40, 763–766.

Dorais, M.J., Whitney, J.A., and Roden, M.F. (1990) Origin of Mafic Enclaves in the Dinkey Creek Pluton, Central Sierra Nevada Batholith, California. Journal of Petrology, 31, 853–881.

Ducea, M.N. (2001) The California arc: Thick granitic batholiths, eclogitic residues, lithospheric-scale thrusting and magmatic flare-ups. Geological Society of America Today, 11, 4–10.

Finch, J.R., Hanchar, J.M., Hoskin, P.W.O., and Burns, P.C. (2001) Rare-earth elements in synthetic zircon: Part 2. A single-crystal X-ray study of xenotime substitution. American Mineralogy, 86, 681–689.

Fliedner, M.M., Klemperer, S.L., and Christensen, N.I. (2000) Three-dimensional seismic model of the Sierra Nevada arc, California, and its implications for crustal and upper mantle composition. Journal of Geophysical Research, 105, 10899–10921.

Frazer, R.E., Lackey, J.S., and Valencia, V.A. (2008) New U-Pb zircon ages of the granites of the Dinkey Dome; reexamining the origins of the Shaver Intrusive Suite. Geological Society of America, Abstracts with programs, 41, pp 14.

616 Frost, B.R., Barnes, C.G., Collins, W.J., Arculus, R.J., Ellis, D.J., and Frost, C.D. (2001) A
617 geochemical classification for granitic rocks. Journal of Petrology, 42, 2033–2048.
618 Fu, B., Page, F.Z., Cavosie, A.J., Fournelle, J., Kita, N.T., Lackey, J.S., Wilde, S.A., and Valley,
619 J.W. (2008) Ti-in-zircon thermometry: applications and limitations. Contributions to
620 Mineralogy and Petrology, 156, 197-215.
621 Glazner, A.F., and Miller, D.M. (1997) Late-stage sinking of plutons. Geology, 25, 1099-1102.
622 Grimes, C.A., John, B.E., Kelemen, P.B., Mazdab, F.K., Wooden, J.L., Cheadle, M.J., Hanghøj,
623 K., and Schwartz, J.J. (2007) Trace element chemistry of zircons from oceanic crust: A
624 method for distinguishing detrital zircon provenance. Geology, 35, 643–646.
625 Guy, R.E. (1980) The Dinkey Creek intrusive series, Huntington Lake Quadrangle, Fresno
626 County, California, 125 p., MS thesis, Virginia Polytechnic Institute, Blacksburg.
627 Guy, R.E., and Wones, D.R. (1980) Petrology of the Dinkey Creek Intrusive Series, Huntington
628 Lake Quadrangle, Fresno County, California. Geological Society of America, Abstracts with
629 programs, 12, pp 440.
630 Halden, N.M., Hawthorne, F.C., Campbell, J.L., Teesdale, W.J., Maxwell, J.A., and Higuchi, D.
631 (1993) Chemical characterization of oscillatory zoning and overgrowths in zircon using 3
632 MeV μ-PIXE. Canadian Mineralogist, 31, 637–647.
633 Halliday, A.N., Stephens, W.E., and Harmon, R.S. (1981) Isotopic and chemical constraints on
634 the development of peraluminous Caledonian and Acadian granites. Canadian Mineralogist,
635 19, 205–216.
636 Hinton, R.W., and Upton, B.G.J. (1991) The chemistry of zircon: variations within and between
637 large crystals from syenite and alkali basalt xenoliths. Geochimica et Cosmochimica Acta,
638 55, 3287–3302.

639 Holland, J.E., Surpless, B., Smith, D.R., Loewy, S.L., and Lackey, J.S. (2013) Intrusive history
640 and petrogenesis of the Ash Mountain Complex, Sierra Nevada batholith, California (USA).
641 Geosphere, 9, 691–717.
642 Hoskin, P.W.O. (2005) Trace-element composition of hydrothermal zircon and the alteration of
643 Hadean zircon from the Jack Hills, Australia. Geochimica et Cosmochimica Acta, 69, 637–
644 648.
645 Hoskin, P.W.O., and Ireland, T.R. (2000) Rare earth element chemistry of zircon and its use as a
646 provenance indicator. Geology, 28, 627 – 630.
647 Hoskin, P.W.O., and Schaltegger, U. (2003) The composition of zircon and igneous
648 metamorphic petrogenesis. Reviews in Mineralogy and Geochemistry, 53, 27–62.
649 Hoskin, P.W.O., Kinny, P.D., Wyborn, D., and Chappell, B.W. (2000) Identifying accessory
650 mineral saturation during differentiation in granitoid magmas: an integrated approach.
651 Journal of Petrology, 41, 1365–1396.
652 Jeon, H., Williams, I.S., and Chappell, B.W. (2012) Magma to mud to magma: rapid crustal
653 recycling by Permian granite magmatism near the eastern Gondwana margin. Earth and
654 Planetary Science Letters, 319-320, 104–117.
655 Kelly, J.L., Fu, B., Kita, N.T., and Valley, J.W. (2007) Optically continuous silcrete quartz
656 cements of the St. Peter Sandstone: High precision oxygen isotope analysis by ion
657 microprobe. Geochimica et Cosmochimica Acta, 71, 3812 – 3832.
658 King, E.M., and Valley, J.W. (2001) The source, magmatic contamination, and alteration of the
659 Idaho batholith. Contributions to Mineralogy and Petrology, 142, 72–88.

660 Kistler, R.W. (1990) Two different lithosphere types in the Sierra Nevada, California. In: J.L.
661 Anderson, Eds., The nature and origin of Cordilleran magmatism, Geological Society of
662 America Memoir, 174, 271–281, Geological Society of America, Boulder.
663 Kistler, R.W., and Peterman, Z.E. (1973) Variations in Sr, Rb, K, Na, and Initial Sr87/Sr86 in
664 Mesozoic Granitic Rocks and Intruded Wall Rocks in Central California. Geological Society
665 of America Bulletin, 84, 3489–3512.
666 Kita, N.T., Ushikubo, T., Fu, B., and Valley, J.W. (2009) High Precision SIMS Oxygen Isotope
667 Analyses and the Effect of Sample Topography. Chemical Geology, 264, 43–57.
668 Kitajima, K., Strickland, A., Spicuzza, M.J., Tenner, T.J., and Valley, J.W. (2016) Improved
669 matrix correction of $\delta^{18}O$ analysis by SIMS for pyralspite and Cr-pyrope garnets.
670 Goldschmidt Conference, 1542, Yokohama, Japan.
671 Lackey, J.S., Valley, J.W., and Saleeby, J.B. (2005) Evidence from zircon for high-δ18O
672 contamination of magmas in the deep Sierra Nevada batholith, California. Earth and
673 Planetary Science Letters, 235, 315–330.
674 Lackey, J.S., Valley, J.W., and Hinke, H.J. (2006) Deciphering the source and contamination
675 history of peraluminous magmas using $\delta^{18}O$ of accessory minerals: examples from garnet-
676 bearing plutons of the Sierra Nevada Batholith. Contributions to Mineralogy and Petrology,
677 151, 20–44.
678 Lackey, J.S., Valley, J.W., Chen, J.H., and Stockli, D.F. (2008) Dynamic Magma Systems,
679 Crustal Recycling, and Alteration in the Central Sierra Nevada Batholith: The Oxygen
680 Isotope Record. Journal of Petrology. 49, 1397–1426.

681 Lackey, J.S., Erdmann, S., Hark, J.S., Nowak, R.M., Murray, K.E., Clarke, D.B., and Valley,
682 J.W. (2011) Tracing garnet origins in granitoid rocks by oxygen isotope analysis: Examples
683 from the South Mountain Batholith, Nova Scotia. Canadian Mineralogist, 49, 417–439.
684 Lackey, J.S., Cecil, M.R., Windham, C.J., Frazer, R.E., Bindeman I.N., and Gehrels, G. (2012)
685 The Fine Gold Intrusive Suite: The Roles of Basement Terranes and Magma Source
686 Development in the Early Cretaceous Sierra Nevada Batholith. Geosphere, 8, 292–313.
687 Lee, C.T., Cheng, X., and Horodyskyj, U. (2006) The development and refinement of continental
688 arcs by primary basaltic magmatism, garnet pyroxenite accumulation, basaltic recharge and
689 delamination: insights from the Sierra Nevada, California. Contributions to Mineralogy and
690 Petrology, 151, 222 - 242.
691 Liggett, D.L. (1990) Geochemistry of the garnet bearing Tharps Peak Granodiorite and its
692 relation to other members of the Lake Kaweah Intrusive Suite, southwestern Sierra Nevada,
693 California In: J.L. Anderson, Eds., The nature and origin of Cordilleran magmatism,.
694 Geological Society of America Memoir, 174, 205-236.
695 Mahood, G.A., Nibler, G.E., and Halliday, A.N. (1996) Zoning patterns and petrologic processes
696 in peraluminous magma chambers: Hall Canyon pluton, Panamint Mountains, California.
697 Geological Society of America Bulletin, 108, 437–453.
698 Memeti, V., Paterson, S., Matzel, J., Mundil, R., and Okaya, D. (2010) Magmatic lobes as
699 “snapshots” of magma chamber growth and evolution in large, composite batholiths: an
700 example from the Tuolumne Intrusion, Sierra Nevada, CA, Geological Society of America
701 Bulletin, 122, 1912–1931.
702 Miller, C.F., McDowell, S.M., and Mapes, R.W. (2003) Hot and cold granites? Implications of
703 zircon saturation temperatures and preservation of inheritance. Geology, 31, 529–532.

Moore, J.G., and Dodge, F.C.W. (1980) Late Cenozoic volcanic rocks of the southern Sierra Nevada, California: Part I. Geology and Petrology summary. Geological Society of America Bulletin, 91, 515–518.

Nelson, W.R., Dorais, M.J., Christiansen, E.R., and Hart, G.L. (2013) Petrogenesis of Sierra Nevada plutons inferred from Sr, Nd, and O isotopic signatures of mafic igneous complexes in Yosemite Valley, California. Contributions to Mineralogy and Petrology, 165, 397–417.

O'Neil, J.R. and Chappell, B.W. (1977) Oxygen and hydrogen isotope relation in the Berridale batholith. Journal of the Geological Society, 133, 559–571.

Ortiz, D.M. (2010) Mineral inclusions in zircons: A tool for provenance analysis of sedimentary rocks, MS thesis, University of Wisconsin, Madison, pp.44.

Page, F.Z., Fu, B., Kita, N.T., Fournelle, J., Spicuzza, M.J., Schulze, D.J., Viljoen, F., Basei, M.A.S., and Valley, J.W. (2007a) Zircons from kimberlite: new insights from oxygen isotopes, trace element, and Ti in zircon thermometry. Geochimica et Cosmochimica Acta 71, 3887–3903.

Page, F.Z., Ushikubo, T., Kita, N.T., Riciputi, L.R., and Valley, J.W. (2007b) High precision oxygen isotope analysis of picogram samples reveals 2-μm gradients and slow diffusion in zircon. American Mineralogist, 92, 1772–1775.

Page, F.Z., Kita, N.T., *and* Valley, J.W. (2010) Ion microprobe analysis of oxygen isotopes in garnets of complex chemistry. Chemical Geology, 270, 9–19.

Patiño Douce, A.E., and Johnston, A.D. (1991) Phase equilibria and melt productivity in the pelitic system: implications for the origin of peraluminous granitoids and aluminous granulites. Contributions to Mineralogy and Petrology, 107, 202–218.

726 Peck, D.L., and Van Kooten, G. (1983) Merced Peak Quadrangle, Central Sierra Nevada,
727 California-Analytic Data. US Geological Survey Professional Paper 1170-D, 29 p.
728 Ratajeski, K., Glazner, A.F., and Miller, B.V. (2001) Geology and geochemistry of mafic to
729 felsic plutonic rocks in the cretaceous intrusive suite of Yosemite Valley, California.
730 Geological Society of America Bulletin, 113, 1485–1602.
731 Ratajeski, K., Sisson, T.W., and Glazner, A.F. (2005) Experimental and geochemical evidence
732 for derivation of the El Capitan Granite, California, by partial melting of hydrous
733 gabbroic lower crust. Contributions to Mineralogy and Petrology, 149, 713–734.
734 Russell, A.K., Kitajima, K., Strickland, A., Medaris Jr., L.G., Schulze, D.J., and Valley, J.W.
735 (2013) Eclogite-facies Fluid Infiltration: Constraints from $\delta^{18}O$ Zoning in Garnet.
736 Contributions to Mineralogy and Petrology, 165, 103–116.
737 Ryan-Davis, J., Lackey, J.S., Gevedon, M., Barnes, J.D., Lee, C.T., Kitajima, K., and Valley,
738 J.W. (2019) Andradite skarn garnet records of exceptionally low $\delta^{18}O$ values within an
739 Early Cretaceous hydrothermal system, Sierra Nevada, CA. Contributions to Mineralogy
740 and Petrology, 174, 68, 1–19.
741 Saleeby, J., Ducea, M., and Clemens Knott, D. (2003) Production and loss of high-density
742 batholithic root, southern Sierra Nevada, California. Tectonics, 22.
743 Sawka, W.N., and Chappell, B.W. (1988) Fractionation of uranium, thorium and rare earth
744 elements in a vertically zoned granodiorite: Implications for heat production distributions in
745 the Sierra Nevada batholith. Geochimica et Cosmochimica Acta, 52, 1131–1143.
746 Scaillet, B., Whittington, A., Martel, C., Pichavant, H., and Holtz, F. (2000) Phase equilibrium
747 constraints on the viscosity of silicic magmas II: implications for mafic-silicic mixing
748 processes. Transactions of the Royal Society of Edinburgh-Earth Sciences, 91, 61-72.

749 Scaillet, B., Holtz, F., and Pichavant, M. (2016) Experimental Constraints on the Formation of
750 Silicic Magmas. Elements, 12, 109-114.
751 Sisson, T.W., Ratajeski, K., Hankins, W.B. et al. (2005) Voluminous granitic magmas from
752 common basaltic sources. Contributions to Mineralogy and Petrology, 148, 635–661
753 Shaw, S.E., Todd, V.R., and Grove, M. (2003) Jurassic peraluminous gneissic granites in the
754 axial zone of the Peninsular Ranges, Southern California, in S. E. Johnson, S. R. Paterson, J.
755 M. Fletcher, G. H. Girty, D. L Kimbrough., and B. A. Martin, Eds., Tectonic evolution of
756 northwestern Mexico and the Southwestern USA, pp. 157–183, Geological Society of
757 America Special Paper, Boulder, Colorado.
758 Speer, J.A. (1982) Zircon. Reviews in Mineralogy, 5, 67–112.
759 Spicuzza, M.J., Valley, J.W., and McConnell, V.S. (1998) Oxygen isotope analysis of whole
760 rock via laser fluorination: an air-lock approach. Geological Society of America, Abstracts
761 with programs, 30, 80.
762 Taylor, H.P. and Sheppard, S.M.F. (1986) Igneous Rocks: 1. Processes of Isotopic Fractionation
763 and Isotope Systematics. Reviews in Mineralogy and Petrology, 16, 227–272.
764 Tobisch, O.T., Renne, P.R., and Saleeby, J.B. (1993) Deformation resulting from regional
765 extension during pluton ascent and emplacement, central Sierra Nevada, California. Journal
766 of Structural Geology, 15, 609–628.
767 Tobisch, O.T., Fiske, R.S., Saleeby, J.B., Holt, E., and Sorensen, S.S. (2000) Steep tilting of
768 metavolcanic rocks by multiple mechanisms, central Sierra Nevada, California. Geological
769 Society of America Bulletin, 112, 1043-1058.

770 Ushikubo, T., Kita, N.T., Cavosie, A.J., Wilde, S.A., Rudnick, R.L., and Valley, J.W. (2008)
771 Lithium in Jack Hills zircons: Evidence for extensive weathering of Earth's earliest crust.
772 Earth and Planetary Science Letters, 272, 666–676.
773 Valley, J.W. (2003) Oxygen isotopes in zircon. Reviews in Mineralogy and Geochemistry, 53,
774 343–385.
775 Valley, J.W., and Kita, N.T. (2009) In situ Oxygen Isotope Geochemistry by Ion Microprobe. In
776 M. Fayek M., Eds., MAC Short Course: Secondary Ion Mass Spectrometry in the Earth
777 Sciences, 41, 19–63.
778 Valley, J.W., Kitchen, N.E., Kohn, M.J., Niendorf, C.R., and Spicuzza, M.J. (1995) UWG-2, A
779 garnet standard for oxygen isotope ratio: strategies for high precision and accuracy with laser
780 heating. Geochimica et Cosmochim Acta, 59, 5223–5231.
781 Valley, J.W., Lackey, J.S., Cavosie, A.J., Clechenko C.C., Spicuzza M.J., Basei M. A. S.,
782 Bindeman, I., Ferreira V., Sial A. N., King E. M., Peck W. H., Sinha A. K., and Wei C. S.
783 (2005) Contributions to Mineralogy and Petrology, 150, 561–580.
784 Vielzeuf, D., Veschambre, M., and Brunet, F. (2005) Oxygen isotope heterogeneities and
785 diffusional profiles in composite metamorphic/magmatic garnets from the Pyrenees.
786 American Mineralogist, 90, 462–472.
787 Villaros, A., Stevens, G., Moyen, J.F., and Buick, I.S. (2009) The trace element compositions of
788 S-type granites: evidence for disequilibrium melting and accessory phase entrainment in the
789 source. Contributions to Mineralogy and Petrology, 158, 543–561.
790 Watson, E.B., and Cherniak, D.J. (1997) Oxygen diffusion in zircon. Earth and Planetary
791 Science Letter, 148, 527–544.

792 Wenner J.M, and Coleman, D.S. (2004) Magma mixing and Cretaceous crustal growth: geology
793 and geochemistry of granites in the central Sierra Nevada Batholith, California. International
794 Geology Review, 46, 880-903.
795 Wiedenbeck, M., Hanchar, J.M., Peck, W.H., Sylvester, P., Valley, J.W., Whitehouse, M., Kronz
796 A., Morishita, Y., Nasdala, L., Fiebig, J., and others (2004) Further Characterisation of the
797 91500 Zircon Crystal. Geostandards and Geoanalytical Research, 28, 9–39.
798 Wones, D.R., Hon, R., and Bateman, P.C. (1969) Depth of crystallization of a garnet-bearing
799 quartz monzonite of the Sierra Nevada Batholith. Eos Transactions, American Geophysical
800 Union, 50, 329.
801 Wright, K., Freer, R., Catlow, C.R.A. (1995) Oxygen diffusion in grossular and some geological
802 implications. American Mineralogist, 80, 1020–1025.
803 Zen, E. (1988) Phase relations of peraluminous granitic rocks and their petrogenetic
804 implications. Annual Reviews in Earth and Planetary Science, 16, 21–51.
805 Zeng, L., Ducea, M., and Saleeby, J.B. (2005) Geochemical characteristics of crustal anatexis
806 during the formation of migmatite at the southern Sierra Nevada, California. Contributions to
807 Mineralogy and Petrology, 150, 386–402.

808 **List of figure captions**

809 Figure 1. Generalized map of the Central Sierra Nevada region, showing the location of
810 peraluminous plutons and the study area, Dinkey Dome granite. Initial $^{87}Sr/^{86}Sr$=0.706 and
811 PA/NA= Panthalassan/North American Break from Kistler (1990). The high $\delta^{18}O$(Zrn) (6.5-
812 7.5‰) and low $\delta^{18}O$(Zrn) (5.5-6.5‰) domains of the central Sierra Nevada intrusives are
813 modified from Lackey et al. (2006, 2008).

Figure 2. Geologic map of the Dinkey Dome with sample sites from this study and Lackey et al. (2006). Map after Bateman and Wones (1972).

Figure 3. Garnet and associated minerals in the Dinkey Dome granite. Sample 10DD02a. Images a and b were taken under transmitted light (PPL= Plain polarized light, XPL= Cross polarized light). Image c is a backscattered electron image (BSE) and shows quartz, muscovite, apatite, ilmenite and zircon, included in a typical garnet from the Dinkey Dome pluton. Values of $\delta^{18}O$ for this garnet are shown in Fig. 7.

Figure 4. Cathodoluminescence (CL) images of zircon grains from grain mounts 1S51-1S82 (Transect A-A' Fig. 2). Circles represent SIMS spots and numbers represent oxygen isotope ratios ($\delta^{18}O$). SIMS spots are 10 μm; scale bars are 50μm.

Figure 5. Cation composition of garnet phenocrysts from grain mounts and thin sections. (a) Almandine–spessartine–pyrope ternary plot includes garnet from both sides of the Dinkey Dome, showing that east side garnet is closer to the almandine-spessartine binary than garnet from the western half. (b) Representative rim-to-rim zoning profiles through the cores of garnets from samples 10DD06b-05 (west) and 10DD19c-02 (east). Background information for data presented in this figure can be found in supplementary data table B.

Figure 6. Oxygen isotope ratios in zircon (a) and garnet (b), and (c) Δ18O (Grt_{Ave}-Zrc_{Ave}) from a traverse of the Dinkey Dome pluton (A-A' in Fig. 2) measured by ion microprobe (this study) and laser fluorination data of Lackey et al. (2006). Data represents zircon and garnet from grain mounts (1S51-1S82) and thin sections (10DD-02-10DD-19). Samples on x-axis are spaced according to relative distance of their field localities. See figure 2 for sample localities. Background information for data presented in this figure can be found in supplementary data tables A, C-D.

Figure 7. Example of a rim-rim traverse of oxygen analyses for a single garnet (10DD-02a-13, BSE image in thin section, see Fig. 3) measured by SIMS. Note the image is rotated ~90° from figure 3.

Figure 8. Chondrite normalized REE patterns for zircons from four samples measured by SIMS (a. 1S82, b. 1S53, c. 1S79, d. 1S77) from the Dinkey Dome (1S82 and 1S79 from the west side, 1S53 and 1S77 from the east side). Filled symbols are from cores and open symbols are rims. Background information for data presented in this figure can be found in supplementary data Table F.

Figure 9. (a) $(Sm/La)_N$ vs. La (ppm) in rims and cores of zircon in the Dinkey Dome, from the same four samples from figure 8 (1S82, 1S53, 1S79, 1S77). (b) Ce/Ce* vs. $(Sm/La)_N$ in rims and cores from zircon in the Dinkey Dome, from the same four samples as in (a). Magmatic and hydrothermal fields from Hoskin (2005) and Grimes et al. (2007). Background information for data presented in this figure can be found in supplementary data Table E.

Figure 10. Evolution of $\delta^{18}O$ of zircon and garnet in the Dinkey Dome pluton recording assimilation and fractional crystallization through time for the (a) western and (b) eastern sides of the pluton.

Figure 11. Model of the genesis of the Dinkey Dome pluton from the earliest stage (I) increments of melt transiting wallrocks of different $\delta^{18}O$ in the presence of early stage zircon, to (IV) final stage crystallization of garnet in the composite pluton.

This is the peer-reviewed, final accepted version for American Mineralogist, published by the Mineralogical Society of America.
The published version is subject to change. Cite as Authors (Year) Title. American Mineralogist, in press.
DOI: https://doi.org/10.2138/am-2021-7472. http://www.minsocam.org/

Table 1. Oxygen isotope data summary.

Sample	Lithology	$\delta^{18}O$ WR ‰ VSMOW (laser)	$\delta^{18}O$ Zrn ‰ VSMOW (laser)	$\delta^{18}O$ Zrn ‰ VSMOW (SIMS)	$\delta^{18}O$ Grt ‰ VSMOW (laser)	$\delta^{18}O$ Grt_{Ave} ‰ VSMOW (SIMS)	$\Delta^{18}O$ (Grt_{Ave}-Zrc_{Ave})
1S51	granite	9.71*	7.76*	C=7.6, R=7.3	6.9	6.2	-1.4
1S52	granite	9.80*	7.51*	C=7.8, R=6.7	7.4	5.9	-1.3
1S53	granite	9.57*	7.53*	C=7.9, R=6.4	6.9	5.9	-1.4
1S54	granite	9.90*	7.81*	C=8.0, R=6.8		6.4	-1.0
1S58	granite	9.90*	7.77*	C=7.5, R=7.0		7.4	0.1
1S77	granite	9.81*	7.63*	C=7.6, R=6.5	6.9	7.0	-0.4
1S79	granite	9.96*	7.67*	C=7.6, R=6.8	7.7	7.5	0.2
1S80	granite	10.30*	7.72*	C=8.1, R=6.3	7.9	7.3	0.1
1S81	granite	9.79*	7.76*	C=7.7, R=7.1	7.2	7.4	0.0
1S82	granite	9.79*	7.73*	C=7.8, R=7.3	8.0	7.6	-0.1
10DD-02	granite	10.47		7.9**		7.1	-0.8
10DD-05	granite	10.14		7.4**		6.7	-0.7
10DD-06	granite	9.65					
10DD-07	granite	9.41					
10DD-08	granite	9.48					
10DD-10	bt hornfel	12.72					
10DD-15	quartzite	11.82					
10DD-16	granite	9.35		7.6**		5.7	-1.9
10DD-17	granite	9.12		6.9**		5.1	-2.0
10DD-18	granite	8.96					
10DD-19	granite	9.06		7.0**		5.0	-2.0
10DD-20	enclave	8.25					
10DD-21	granite	9.17					
10DD-22	granite	9.06					

*Lackey et al. (2006) oxygen isotope analyses by Laser Fluorination.
**SIMS analyses on grains too small to distinguish core vs. rim.
C=Core, R=Rim; Zrn=Zircon, Grt=Garnet, WR=Whole Rock.
Samples 1S51 - 1S82 are grain mounts; 10DD-02 - 10DD-22 are thin sections.

Supplementary Data Tables:

Supplementary Table A: Sample locations and $\delta^{18}O$ summary.

Supplementary Table B: EPMA data.

Supplementary Table C: Zircon SIMS $\delta^{18}O$ data.

Supplementary Table D: Garnet SIMS $\delta^{18}O$ data.

Supplementary Table E: Garnet Laser Fluorination $\delta^{18}O$ data.

Supplementary Table F: Zircon REE data.

This is the peer-reviewed, final accepted version for American Mineralogist, published by the Mineralogical Society of America.
The published version is subject to change. Cite as Authors (Year) Title. American Mineralogist, in press.
DOI: https://doi.org/10.2138/am-2021-7472. http://www.minsocam.org/

Fig. 1

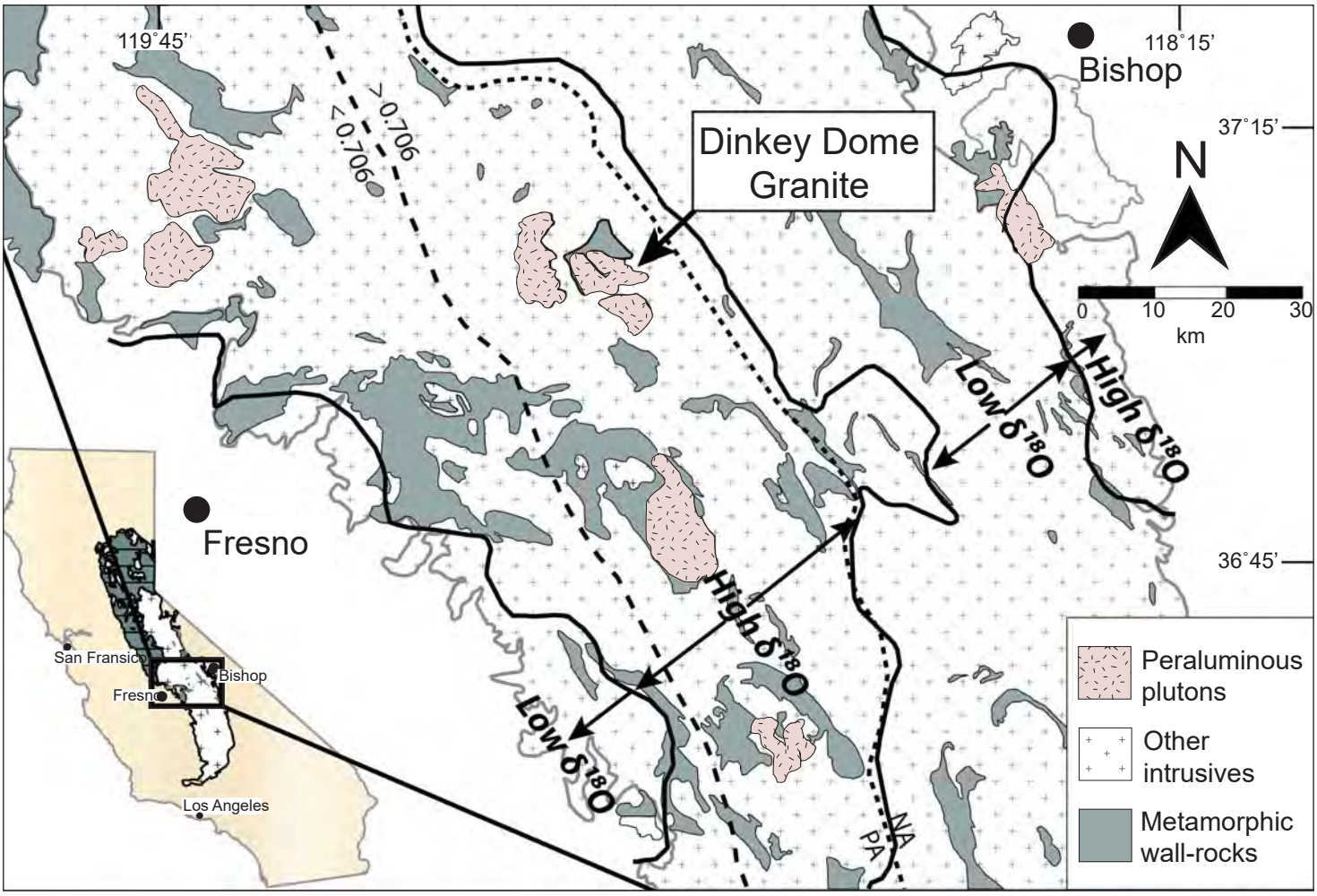

This is the peer-reviewed, final accepted version for American Mineralogist, published by the Mineralogical Society of America.
The published version is subject to change. Cite as Authors (Year) Title. American Mineralogist, in press.
DOI: https://doi.org/10.2138/am-2021-7472. http://www.minsocam.org/

Fig. 2

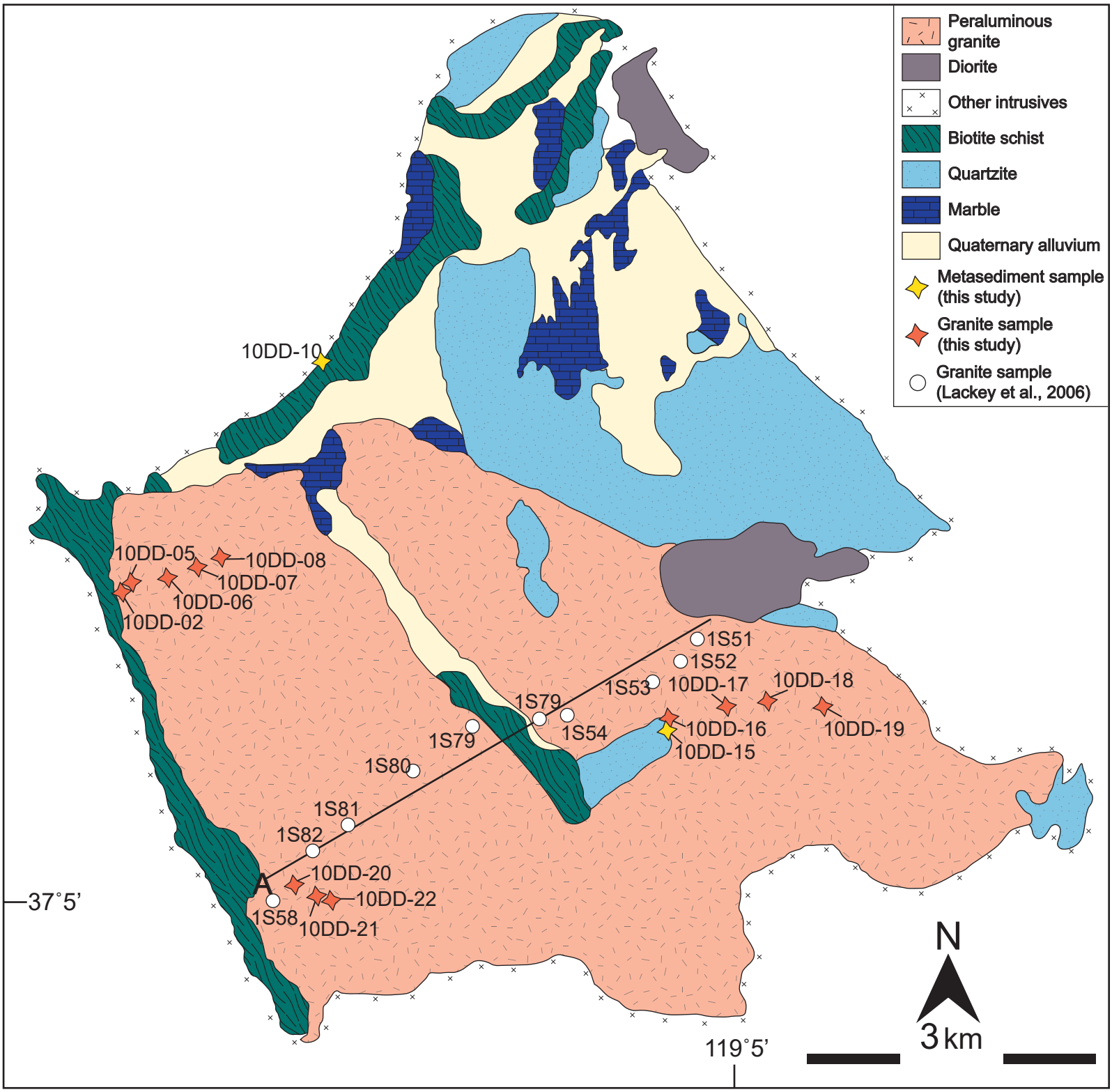

Fig. 3

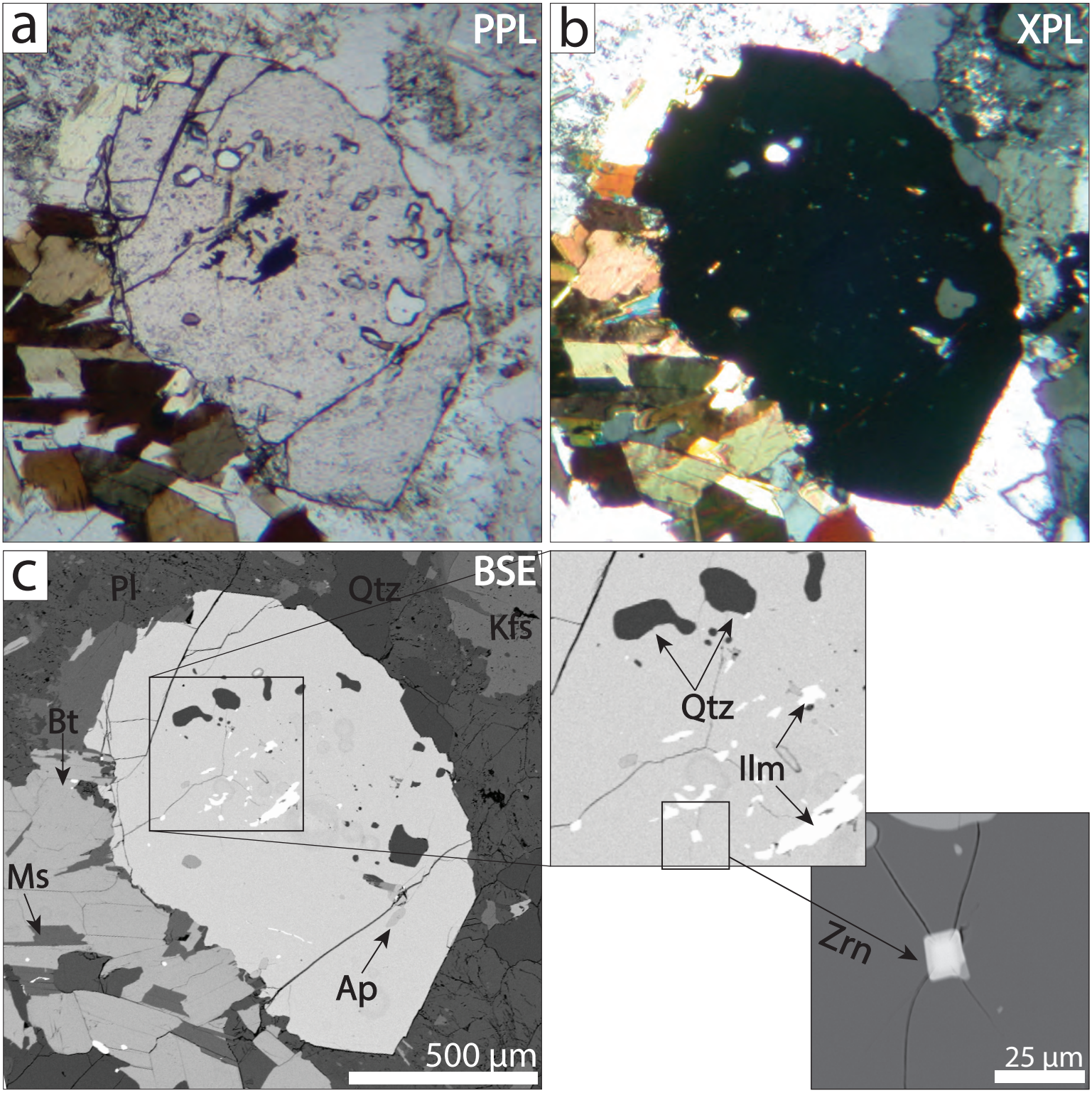

This is the peer-reviewed, final accepted version for American Mineralogist, published by the Mineralogical Society of America.
The published version is subject to change. Cite as Authors (Year) Title. American Mineralogist, in press.
DOI: https://doi.org/10.2138/am-2021-7472. http://www.minsocam.org/

Fig. 4

This is the peer-reviewed, final accepted version for American Mineralogist, published by the Mineralogical Society of America.
The published version is subject to change. Cite as Authors (Year) Title. American Mineralogist, in press.
DOI: https://doi.org/10.2138/am-2021-7472. http://www.minsocam.org/

Fig. 5

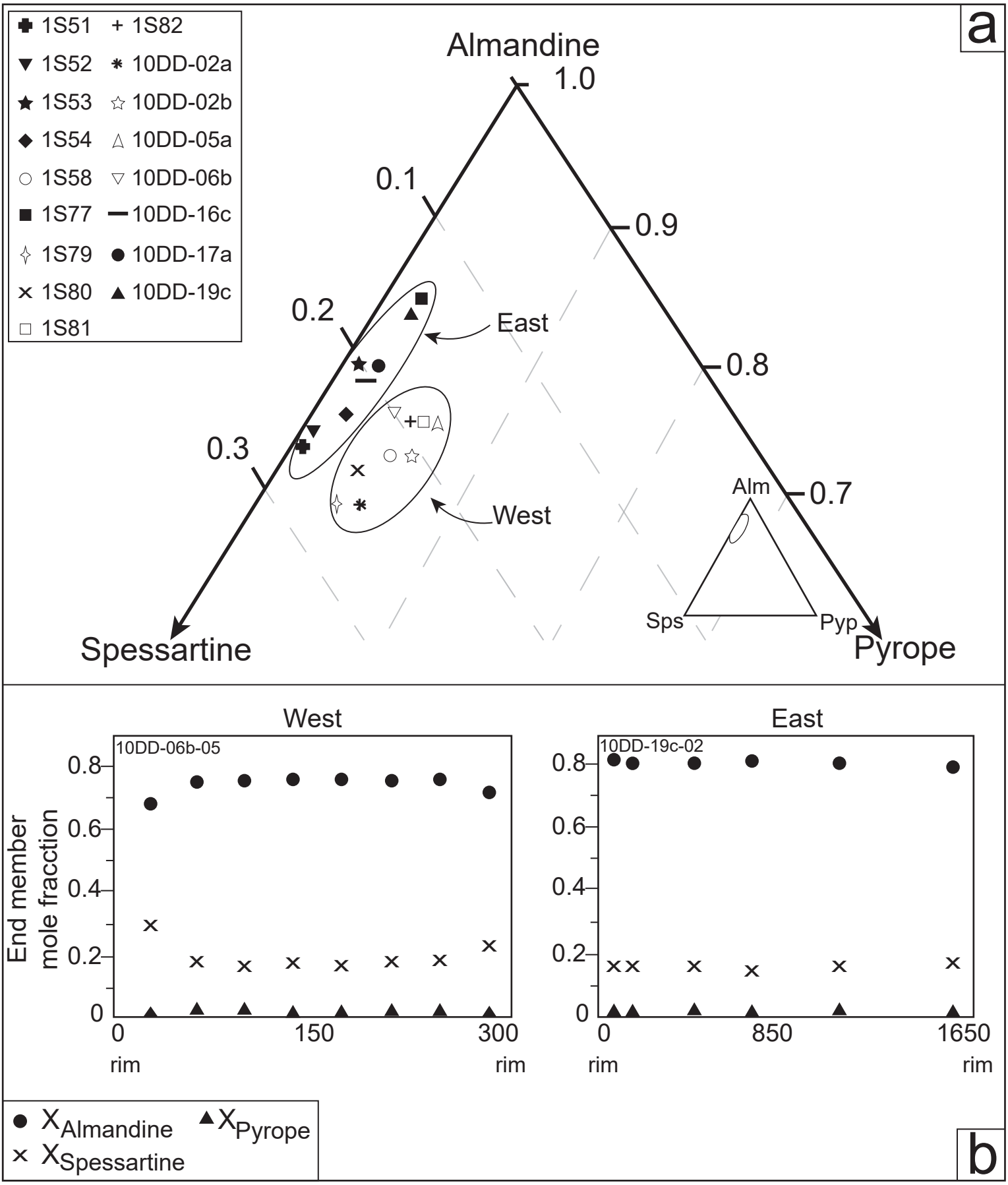

This is the peer-reviewed, final accepted version for American Mineralogist, published by the Mineralogical Society of America.
The published version is subject to change. Cite as Authors (Year) Title. American Mineralogist, in press.
DOI: https://doi.org/10.2138/am-2021-7472. http://www.minsocam.org/

Fig. 6

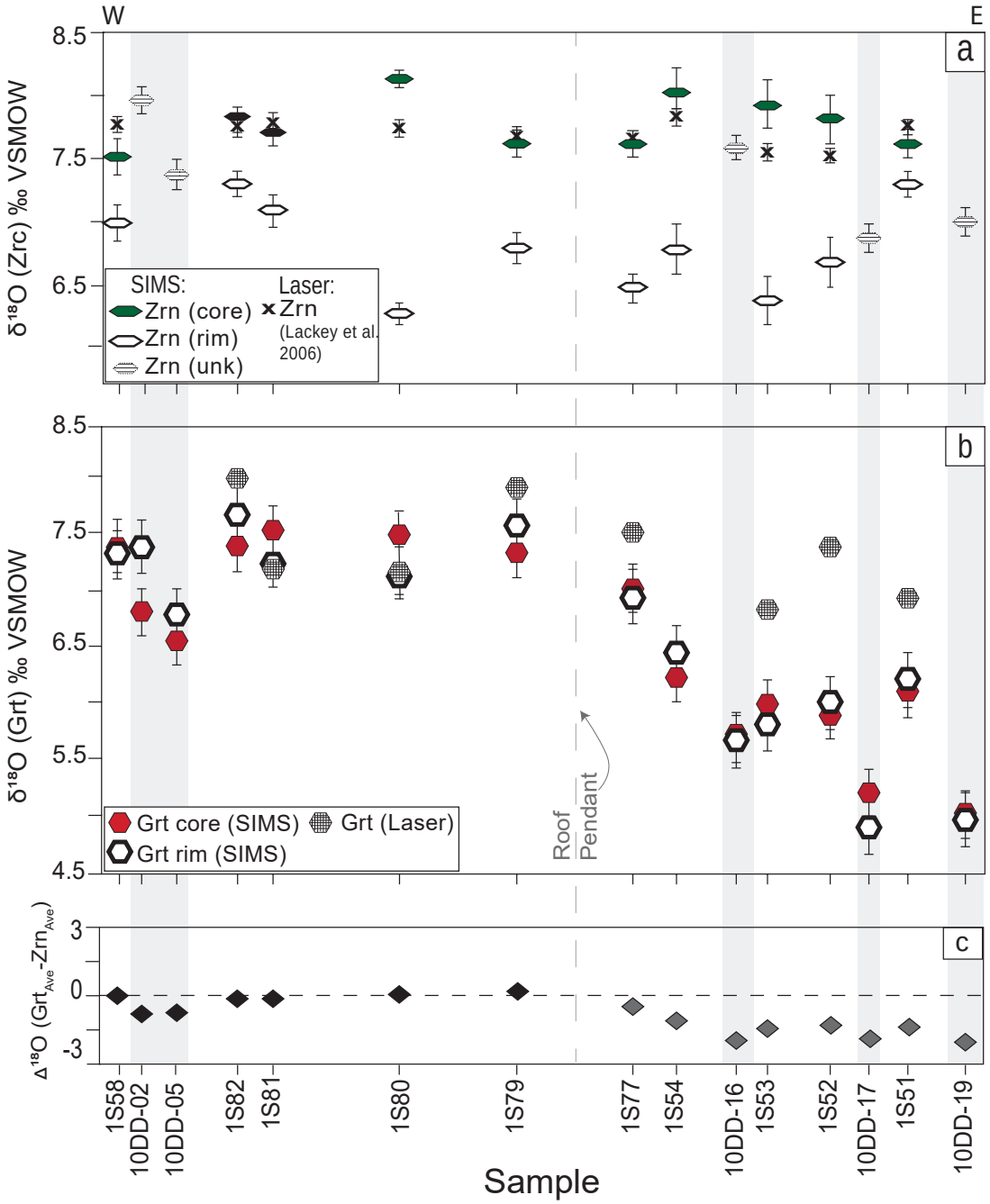

This is the peer-reviewed, final accepted version for American Mineralogist, published by the Mineralogical Society of America.
The published version is subject to change. Cite as Authors (Year) Title. American Mineralogist, in press.
DOI: https://doi.org/10.2138/am-2021-7472. http://www.minsocam.org/

Fig. 7

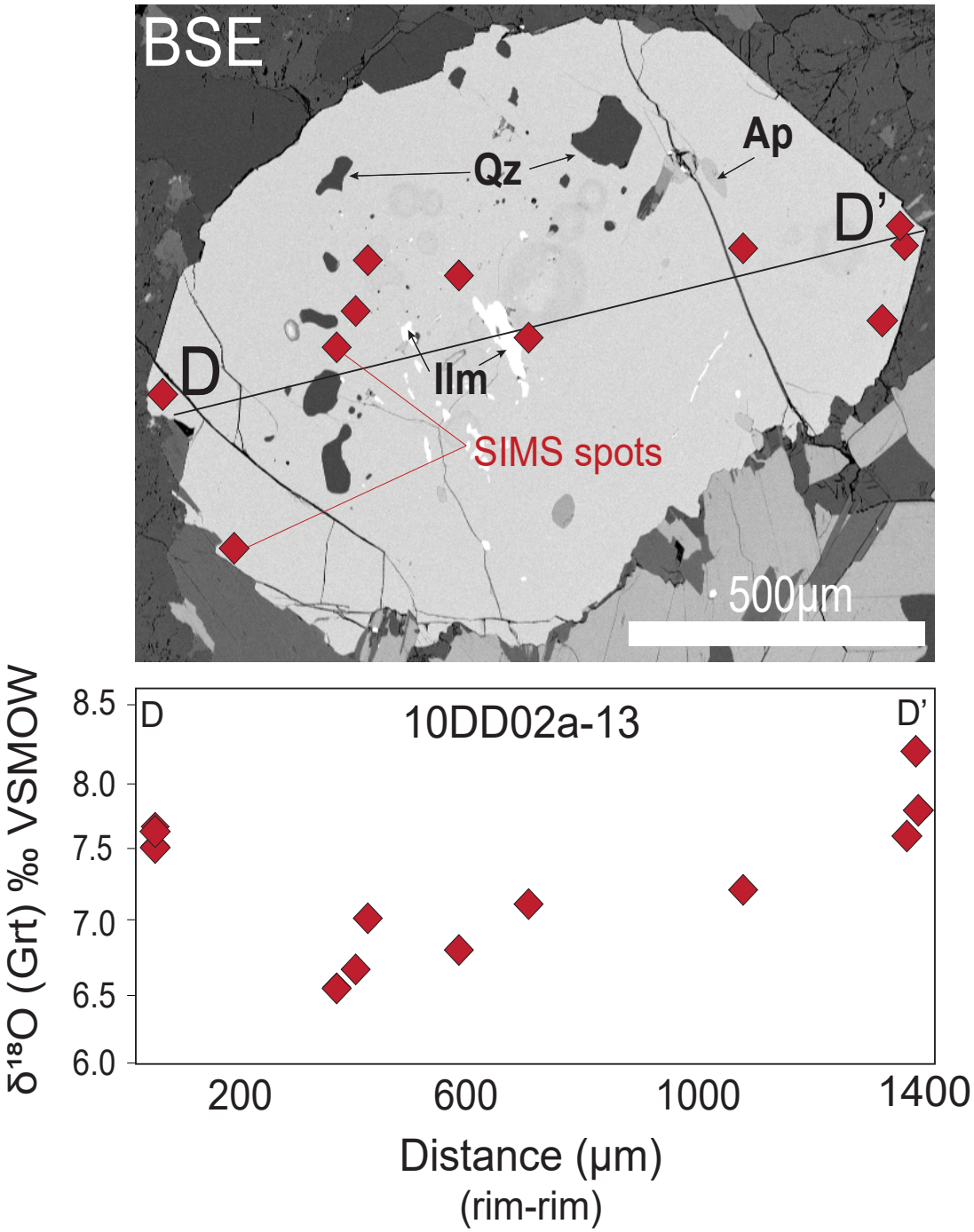

This is the peer-reviewed, final accepted version for American Mineralogist, published by the Mineralogical Society of America.
The published version is subject to change. Cite as Authors (Year) Title. American Mineralogist, in press.
DOI: https://doi.org/10.2138/am-2021-7472. http://www.minsocam.org/

Fig. 8

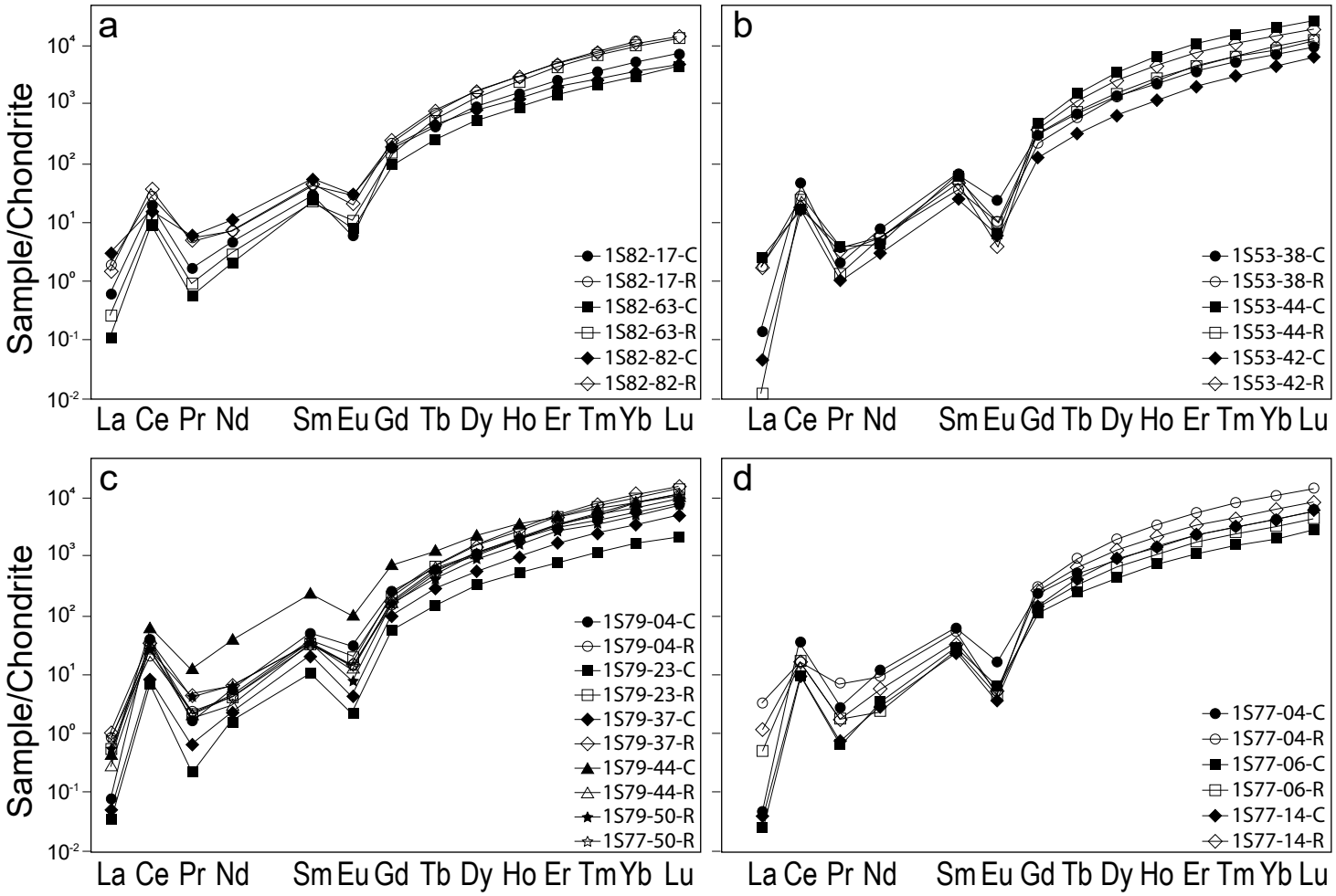

This is the peer-reviewed, final accepted version for American Mineralogist, published by the Mineralogical Society of America.
The published version is subject to change. Cite as Authors (Year) Title. American Mineralogist, in press.
DOI: https://doi.org/10.2138/am-2021-7472. http://www.minsocam.org/

Fig. 9

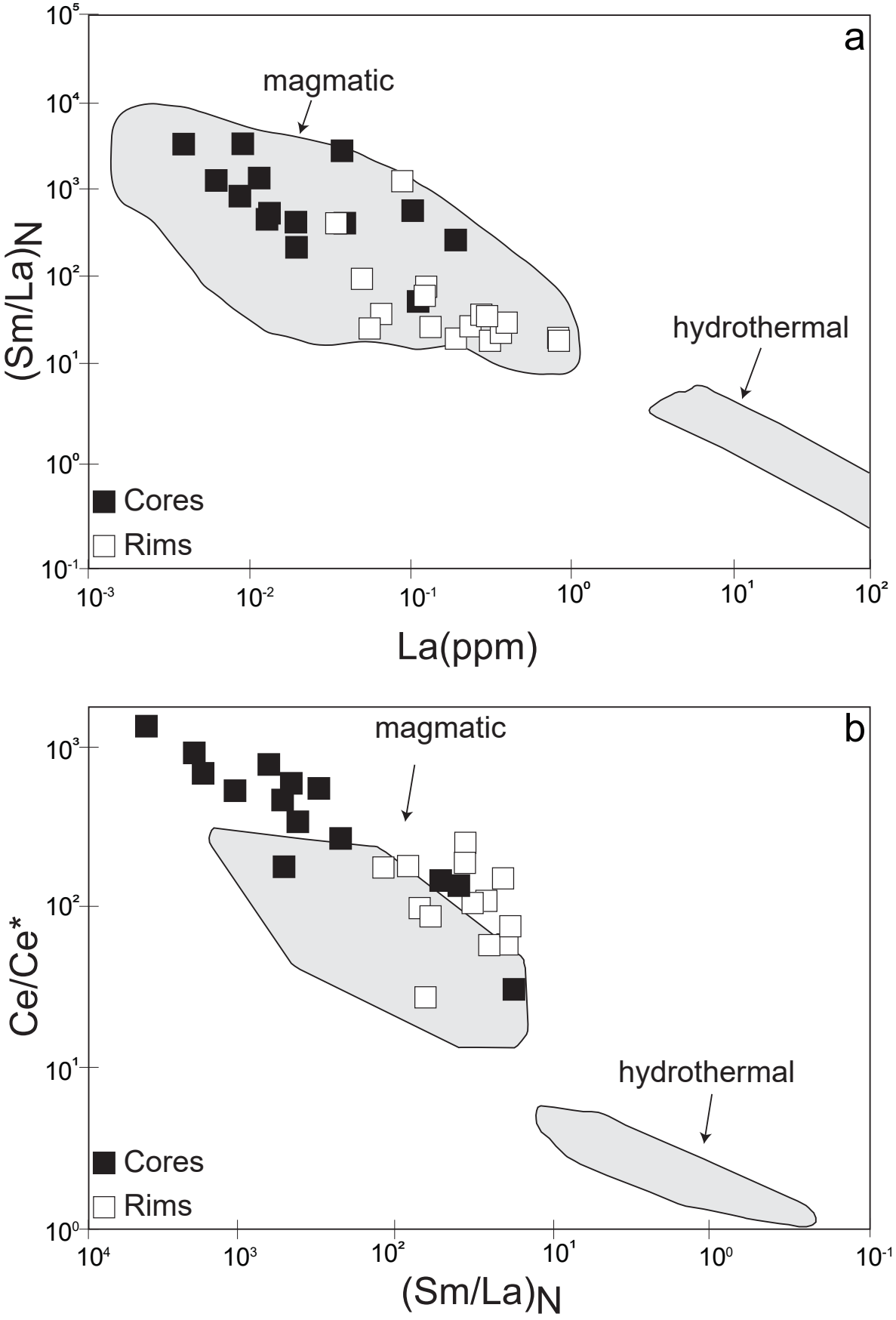

This is the peer-reviewed, final accepted version for American Mineralogist, published by the Mineralogical Society of America.
The published version is subject to change. Cite as Authors (Year) Title. American Mineralogist, in press.
DOI: https://doi.org/10.2138/am-2021-7472. http://www.minsocam.org/

Fig. 10

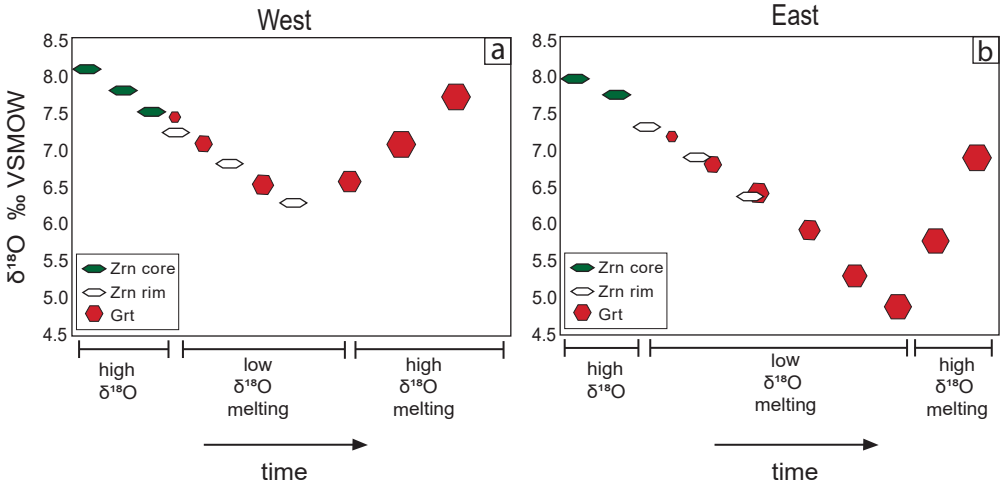

Fig 11